ACS OMEGA

Article

Cite This: ACS Omega 2019, 4, 8255−8273

http://pubs.acs.org/journal/acsodf

Formation of Surface Deposits on Steel and Titanium Aviation Fuel Tubes under Real Operating Conditions

Igor Velkavrh,*[,‡] Ion Palamarciuc,[§] Dan Gelu Galuşcă,[§] Alexander Diem,[‡] Josef Brenner,[∥] Christoph Gabler,[∥,†] Brian Mellor,[⊥] and Monica Ratoi[⊥]

[‡]V-Research GmbH, Stadtstrasse 33, 6850 Dornbirn, Austria

[§]Faculty of Materials Science and Engineering, Gheorghe Asachi Technical University of Iaşi, Bulevardul Profesor Dimitrie Mangeron 67, Iaşi 700050, Romania

[∥]AC2T research GmbH, Viktor Kaplan-Straße 2, 2700 Wiener Neustadt, Austria

[⊥]National Centre for Advanced Tribology (nCATS), University of Southampton, Highfield Campus, Southampton SO17 1BJ, U.K.

ABSTRACT: In this study, stainless steel and titanium (Ti) tubes obtained from a turbofan engine after the end of its lifetime were analyzed in order to compare the amount of pyrolytic coke present and its influence on the parent, base material. Various analytical techniques including microhardness and topographical evaluations, optical emission spectrometry (OES), scanning electron microscopy (SEM), energy-dispersive X-ray spectroscopy (EDX), Raman spectroscopy, and X-ray photoelectron spectroscopy (XPS) were applied. On steel surfaces, a thick pyrolytic coke deposition layer consisting of carbon and oxygen and also containing elements from the tube material, fuel, and fuel additives was found. The concentration of elements from the pyrolytic coke continuously decreased with distance from the surface of the deposit, while the concentrations of elements from the tube material continuously increased, with the concentrations of elements from the fuel and the fuel additives being relatively constant. With ultrasonic cleaning in distilled water, most of the deposits could be removed. Only carbon-rich patches with a thickness of more than 300 nm remained adhered to the surface and/or had diffused into the original material. On Ti surfaces, the thickness of the C-rich fuel deposit layer was significantly thinner as compared to that on the stainless steel; however, the surface was covered with an ∼3 μm-thick oxide layer, which consisted of elements from the fuel additives. It is believed that the beneficial properties of Ti covered with a thin layer of TiO_2, such as low adhesion and/or surface energy, have promoted different deposition mechanisms compared to those of stainless steel and thus prevented pyrolytic coke deposition and the related material deterioration observed on stainless steel.

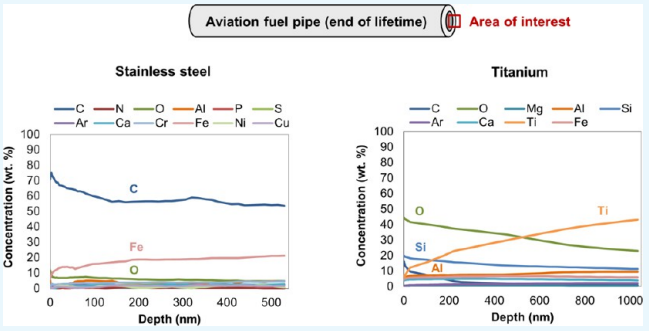

1. INTRODUCTION

The inner surface of aviation fuel tubes can be damaged by the diffusion of fuel species that takes place at elevated temperatures. On the inner surfaces of the tubes, solid pyrolytic coke deposits from kerosene can form, which can degrade the tube material properties due to intergranular corrosion. In combination with thermal fatigue, this can lead to a reduced lifetime or even catastrophic failure of the tubes.

Pyrolytic carbon (C) deposition due to the thermal degradation of hydrocarbon fuels has been studied extensively.[1−4] Several influences of the environment have already been recognized. Temperature is considered to be the primary decisive factor affecting thermal oxidation and pyrolytic coke deposition originating from the thermal decomposition of hydrocarbons.[5,6]

The type of fuel or its composition can markedly affect the type and amount of pyrolytic carbon deposition. DeWitt et al. reported that synthetic paraffinic kerosene is more reactive and provides higher coke deposition rates than petroleum-derived fuels due to a lack of efficient hydrogen donors that act to terminate chain reactions (higher net propagation rate).[7] Sulfur (S) is an undesirable component present in all fossil fuels and has a high corrosion activity. Generally, the detrimental effect of S compounds can be related to their thermal decomposition, leading to hydrogen sulfide, which corrosively attacks nickel−chromium−iron (Ni−Cr−Fe) alloys leading to grain boundary embrittlement.[8] S has also been correlated with the increase of the deposition of carbonaceous materials onto metallic surfaces.[7−10] However, the interaction of S compounds with metal surfaces is very complex. It has been suggested that S compounds in jet fuel can activate the metal surface for C deposition by forming metal sulfides under pyrolytic conditions and thus increase the surface area available for C deposition.[9] On the other hand, it

Received: December 20, 2018
Accepted: March 28, 2019
Published: May 8, 2019

DOI: 10.1021/acsomega.8b03576
ACS Omega 2019, 4, 8255−8273

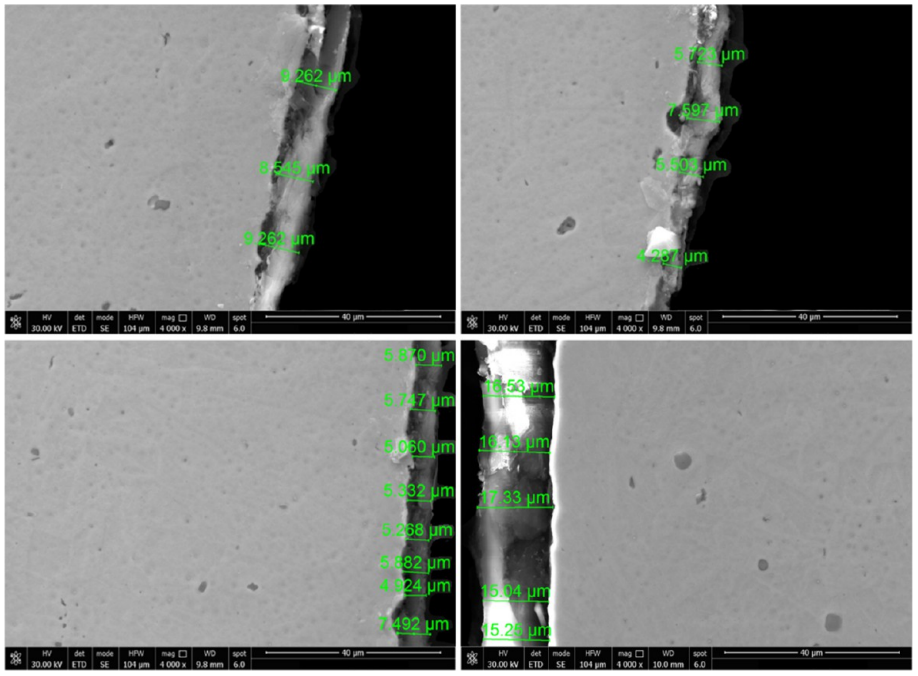

Figure 1. SEM micrographs of the pyrolytic coke deposit layer on the bore of the as-received stainless steel sample showing the thickness of the deposited layer.

was suggested that they can passivate the metal surface by forming sulfides and blocking the active sites.[11] Namely, Venkataraman and Eser showed that reducing the S content of the Jet A fuel from 0.10 to 0.01 wt % inhibited the formation of metal sulfide on the SS316 surface.[9] This consequently inhibited the growth of C film deposits. The amount of heterogeneous phase deposits formed was found to be directly dependent on the surface area of metal sulfides available. Furthermore, it was reported that metal−S interactions may hinder the formation of some types of carbonaceous deposits, especially of the filamentous type.[11,12] On catalytically active substrates, Jet A fuel was less susceptible to producing carbon deposits than JP-8 fuel: the substantially lower amounts of carbon deposition obtained from Jet A fuel under the same thermal stressing conditions were ascribed to the higher concentrations of sulfur and heavy (long-chain) alkane concentrations in Jet A fuel compared to JP-8 fuel.[11] According to the authors, these could have passivated the active sites on metal substrates during thermal stressing through the excessive formation of metal sulfides or encapsulation by thermally produced solid carbons.[11]

The chemical and structural properties of materials are considered important in determining the amount and the rate of pyrolytic coke deposit formation. It has been reported that the highest catalytic activity for carbon deposition is exhibited by iron (Fe), cobalt (Co), nickel (Ni), and alloys containing these elements.[12] The effect of Ni on increasing carbon deposition was observed also by comparing SS316 steel and Inconel 600, where Inconel 600 showed significantly higher deposition.[9] Coating of the SS316 steel surface with alumina (Al_2O_3) further reduced C deposition. Altin and Eser conducted thermal stressing of JP-8 fuel in an isothermal flow reactor.[13] They reported that the activity of the tube surfaces toward carbon deposition decreased in the order Ni > SS316 > SS304 > Silcosteel > glass-lined stainless steel. Mohan and Eser investigated the effect of various metal alloys on carbon deposition from Jet A at a wall temperature of 350 °C and a reactor pressure of 3.5 MPa.[4] They related the differences in the activity of the metal substrates observed to their varying reaction with reactive sulfur compounds in the fuel and interaction of oxygenated intermediates formed by autoxidation during thermal stressing. The amount of carbon deposited on the alloys increased in the order: AISI316 < AISI 321 ≈ AISI 304 < Inconel 600 < AISI 347 < Inconel 718 < Fecralloy < Inconel 750-X. The presence of molybdenum, titanium, and niobium in smaller amounts did not appear to affect C deposition under the experimental conditions. C deposition on Fecralloy, Inconel 600, Inconel 718, and Inconel 750-X indicated that the formation of metal sulfides does not necessarily passivate the surface and reduce C deposition as was presumed in previously mentioned studies.[11,12]

Hydrocarbons have been found to promote corrosion activity in aviation tubes; for example, López León et al. analyzed the corrosion behavior of AISI 1018 steel in a buffered solution of chlorides with and without hydrocarbon in a continuous flow rate system.[14] They observed that the presence of hydrocarbons in the system promotes corrosion in comparison to the system in the absence of hydrocarbons (the interaction of chlorides with metal is more favored). In another study, López León et al. investigated the electrochemical behavior of a pyridinic compound, as a corrosion inhibitor, on a system of AISI 1018 carbon steel in a synthetic corrosive medium, in the absence and presence of hydrocarbons (kerosene).[15] They reported that the inhibitor efficiency decreased with the presence of hydrocarbons in the system. In the presence of hydrocarbons, steel showed higher activity; that is, the interactions between the chlorides in the solution and metal were favored by the presence of hydrocarbons.

Although various published studies have investigated the properties of pyrolytic coke deposits formed on different materials, fuels, and thermal stressing conditions, these coke deposits were formed under narrowly defined laboratory

DOI: 10.1021/acsomega.8b03576
ACS Omega 2019, 4, 8255−8273

conditions, often by applying experimental parameters that accelerated their formation and over relatively short time intervals (typically in the range of 10 to 20 h). In the available literature, very few case studies and studies focused on the analysis of deposits from a real mechanical system can be found. Furthermore, T-1 and TS-1 jet fuels, which have unique components and characteristics as compared to other jet fuels, have been seldom investigated. The objective of this study is to analyze the effect of tube material on pyrolytic coke deposit formation in a real system using T-1 and TS-1 jet fuels. For this purpose, stainless steel and titanium tubes were taken from an Ivchenko AI-25 twin-shaft medium bypass turbofan engine after the end of its lifetime, and the formation of thermal deposition products and their effect on material degradation on their surfaces were compared.

2. RESULTS

2.1. Structural Analyses. The inner surface of the stainless steel tube was uniformly covered with a black fuel deposit layer as shown by the SEM micrographs (Figure 1). The thickness of the surface deposit layer varied between 4 and 17 μm, and the average thickness was ∼9 μm. On the titanium surface, no visible deposit from the fuel could be observed.

Figure 2 shows that the fuel deposit had penetrated the tube intergranularly up to a depth of ∼10 μm. In the intergranular penetration area, corrosion pits with a depth of 3−4 μm were identified (Figure 3). Topographic analyses on the outer and inner surfaces of the as-received and ultrasonically cleaned stainless steel showed that the surface roughness of the degraded surfaces had an R_z value of ∼10 μm and was significantly higher compared to the external surface of the tubes, which had an R_z value of ∼4 μm (Figure 4).

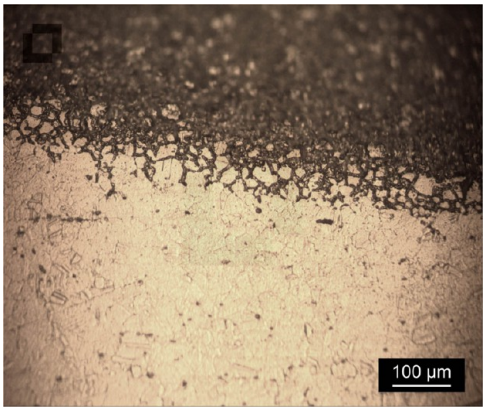

Figure 2. Optical micrograph of the interface between the deposit and the stainless steel tube showing intergranular penetration to a depth of 10 μm.

From Figure 5, it can be seen that the microhardness values along the wall thickness of the stainless steel tube were slightly different in transversal and longitudinal sections. In the transverse section, the microhardness values along the tube wall thickness were more or less constant, that is, within experimental error, while in the longitudinal section, they were linearly increasing from the outer toward the inner tube surface, most probably due to the residual stresses induced by the seamless tube manufacturing process. However; in both sections, similar microhardness values were measured in the end points, that is, near the outer surface (point 1) and the inner surface (point 12, bore) of the tube. Near the outer surface, microhardness was ∼150 HV1, while near the inner surface (bore), a step increase in microhardness to ∼250 HV1 was observed. The increase of hardness is an effect induced by the intergranular corrosion, which typically results in a local increase of microhardness and brittleness of the affected area.

In Figure 6, SEM micrographs of the inner surfaces of the ultrasonically cleaned stainless steel sample are presented. In Figure 6a, the damaged surface at the point of deposit removal is shown, and in Figure 6b, a detail from Figure 6a is presented at higher magnification. Figure 6b reveals that after the removal of the deposit from the inner surface of the stainless steel sample, a high density of microcavities (diameters between 1 and 3 μm) was observed.

In Figure 7, an SEM image of the inner surface of the titanium sample is presented. The surface was covered with a layer of fine particles. EDX analyses on the inner surface of the titanium sample (Table 1) revealed that the surface was covered with an oxide layer and had a Ti concentration of ∼65 wt % and O concentration of ∼24 wt %.

2.2. Chemical Analyses. *2.2.1. Outer Surface of Sample S1.* Figure 8 shows the survey XPS spectra on the outer surface of sample S1 before and after sputtering with Ar^+ ions for 6110 s, and in Table 2, the quantified values derived from these spectra are presented. Before sputtering, a high concentration of C (∼80 wt %) was detected. Additionally, ∼12 wt % O and low concentrations of Si and Ca (∼4 and 3 wt %, respectively) were detected. Obviously, the surface was covered with a layer consisting primarily of C and O. After sputtering to a depth of ∼300 nm (see Table 12 for the approximate depths of material removed during the XPS analyses of the tube samples), the concentrations of all elements, which were detected before sputtering, decreased: the C concentration decreased significantly to ∼8 wt %, O concentration decreased to ∼4 wt %, and Si and Ca concentrations decreased to ∼2.5 and 1 wt %, respectively. After sputtering, the following elements, which were not detected before sputtering, were additionally detected: Ar from sputtering with Ar^+ ions (1.4 wt %) and Fe, Cr, Ni, and Ti from the tube material (at concentrations of ∼60, 13, 8, and 1%, respectively).

From the depth profiles (Figure 9), a gradual decrease of C concentration and a simultaneous increase of Fe and Cr concentrations can be seen, which indicate that the tube material composition was gradually approached. At the final sputtering depth of ∼300 nm, the C concentration was reduced significantly to ∼8 wt %, which indicates that at this depth, the majority of the layer of organic impurities from the oil from the fuel-oil heat exchanger had been removed. With high probability, at this point, the tube material had been reached, and the C detected was due to the so-called "shading effect", which typically occurs with sputtering of rough surfaces or surfaces covered with layers having inhomogeneous thicknesses where at some point, parts of the surface are already "clean", while valleys and sputter shadows are still covered and therefore still detected by the detector. Thus, from the depth profiles, it could be concluded that the thickness of the C-based layer on the outer surface of sample S1 was at most 300 nm.

2.2.2. Deposit Layer on the Inner Surface of Sample S1. Figure 10 shows the XPS spectra on the deposit layer on the inner surface (bore) of sample S1 before and after sputtering with Ar^+ ions for 10610 s, and in Table 3, the quantified values from these spectra are presented. Before sputtering, ∼66 wt %

DOI: 10.1021/acsomega.8b03576
ACS Omega 2019, 4, 8255−8273

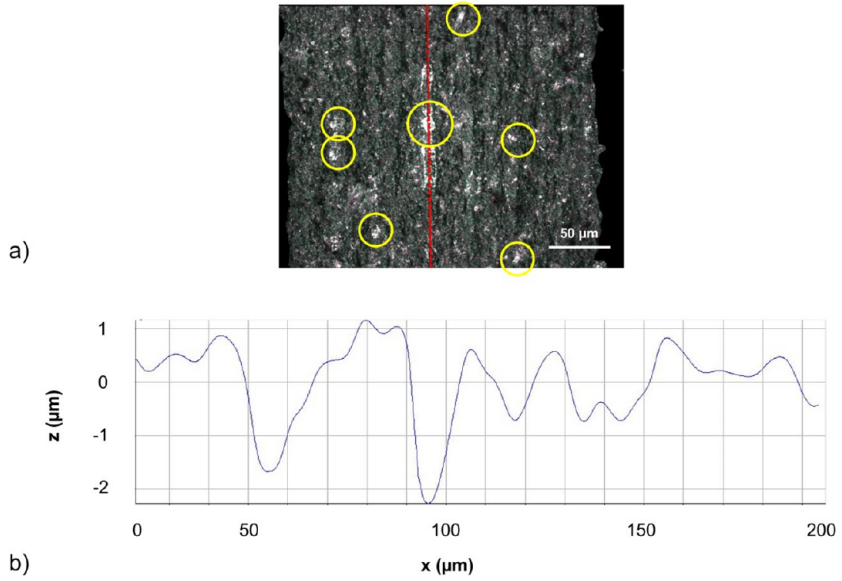

Figure 3. Surface of the ultrasonically cleaned stainless steel sample: (a) corrosion pits on the surface are marked with yellow circles; (b) roughness profile along the red dotted line through a corrosion pit.

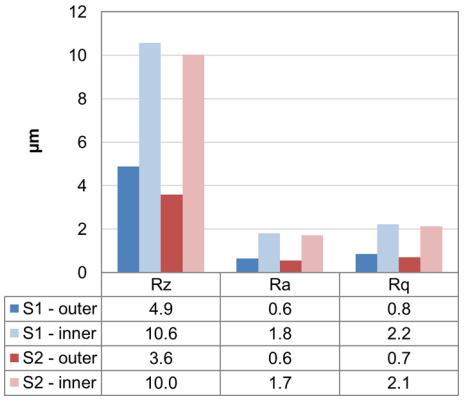

	Rz	Ra	Rq
S1 - outer	4.9	0.6	0.8
S1 - inner	10.6	1.8	2.2
S2 - outer	3.6	0.6	0.7
S2 - inner	10.0	1.7	2.1

Figure 4. Surface roughness parameters R_z, R_a, and R_q measured on the outer and inner surfaces of the as-received (S1) and ultrasonically cleaned (S2) stainless steel samples.

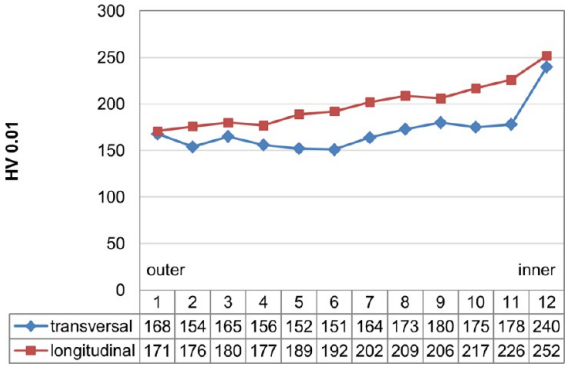

	1	2	3	4	5	6	7	8	9	10	11	12
transversal	168	154	165	156	152	151	164	173	180	175	178	240
longitudinal	171	176	180	177	189	192	202	209	206	217	226	252

Figure 5. Microhardness values through the thickness of the stainless steel tube for transverse and longitudinal cross sections of the stainless steel tube; (1) measured at the outer surface and (12) measured at the inner surface.

of C and ∼17 wt % of O were detected. A low concentration of Fe (4.5 wt %) was also detected. Additionally, N, Al, P, and S were detected in concentrations from ∼2 to 6 wt %. Detailed analyses of the composition of chemical species (Table 4) showed that 31.3 wt % of the C had a binding energy of 283.57 eV where C−C and carbidic C are typically found, 27.9 wt % of the C had a binding energy of 284.66 eV, which is typical for organic aliphatic carbon of C−C or C−H type, and 3.6 wt % of the C had a binding energy of 287.68 eV, which is typical for C−O and C═O bonds. Al was present as Al oxide, P as phosphate, and S as sulfate.

N is an element found in various fuel additives,[16,17] which explains its presence in the surface deposit. By far, the greatest proportion of any fuel additive consists of C, H, O, and often also N. N can be found in deposit control additives, often referred to by the generic term detergents, which consist of molecules such as amides, amines, polybutene succinimides, polyether amines, polyolefin amines, and Mannich amines. N is also found in combustion improvers, which include both ashless and metal-containing additives. Furthermore, hydrogen sulfide (H_2S) "scavengers" can also be based on N polymers that react with H_2S to form low hazard compounds. The origin of Al, more precisely Al oxides, in the surface deposit is most probably also due to the jet fuel. Al nanoparticles have been shown to have the ability to increase the volumetric energy density, decrease ignition delay, increase heat of combustion, and catalyze fuel decomposition of kerosene.[18] It was also reported that the addition of Al_2O_3 nanoparticles to diesel fuel improved its ignition probability,[19] while in biodiesel, it increased the flash point and the calorific value and decreased CO, HC, and NO_x emissions.[20] P may also originate from the fuel additive. Generally, phosphorus-based compounds (and metals such as potassium, sodium, iron, or manganese) can be found in additives used to reduce wear in spark ignition engines.[16] The combusted metal salts act as a protective lubricant and prevent the direct metal-to-metal contact that would otherwise cause high wear.[17] The S concentration in jet fuel T-1 is lower than 0.1 wt % (Table 11). S is an inevitable component present in all mineral oil and/or fossil fuel products since they are derived from decayed animal/organic remains.[21] The total sulfur content in petroleum products is an important variable, as sulfur compounds are associated with problems involved in the storage, processing, transportation, and final

DOI: 10.1021/acsomega.8b03576
ACS Omega 2019, 4, 8255−8273

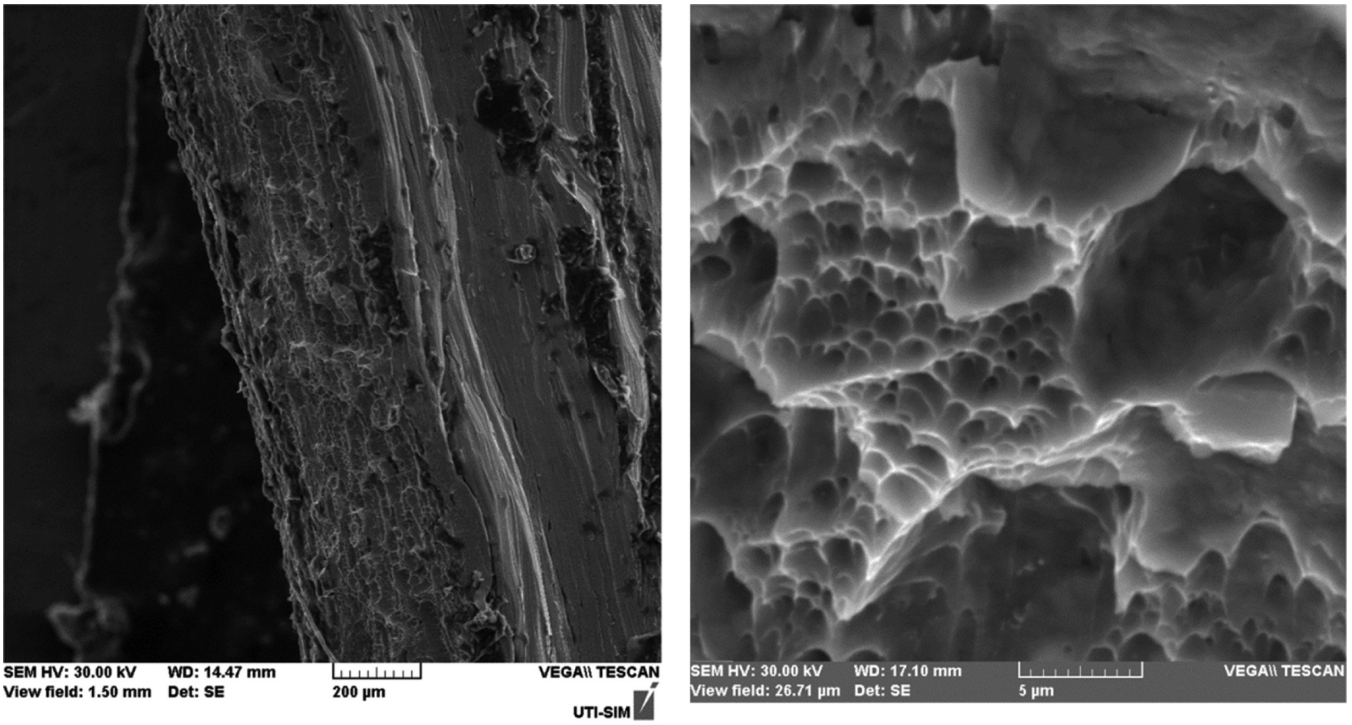

Figure 6. SEM images of inner surfaces of the ultrasonically cleaned stainless steel sample: (a) damaged surface at the point of deposit removal and (b) higher magnification of a detail from (a).

quality of fuel products.[22] Typical problems caused by sulfur compounds are catalyst poisoning and deactivation in processing, corrosion of equipment, and the oxidation of sulfur compounds to SO_x when the fuel is combusted, which causes serious environmental pollution.[23] S is also the element, which might cause intergranular corrosion. As metal sulfides are very different from the corresponding oxides, corrosion by sulfur is generally much more rapid.[24] Specifically, as the sulfide ion is much larger than the oxide, the cation/anion radius ratios in metal oxides are smaller than in the corresponding sulfides. The difference in anion size leads also to M−S bond lengths longer than the corresponding M−O distances. In ionic crystals, this leads to smaller lattice energies for the sulfides, which is reflected in the lower free energies for the sulfide formation and in the generally lower melting points of sulfides.

After sputtering, to a depth of ∼530 nm (Figure 10b and Table 3), the C concentration has slightly decreased to ∼52 wt %, the O concentration decreased to ∼5 wt %, and the Fe concentration increased to ∼21 wt %. The Al concentration remained similar, while P and S concentrations slightly decreased to 2.4 and 1.7 wt %, respectively. Apart from the elements detected already before sputtering, the following elements were additionally detected: Ar from sputtering with Ar^+ ions (2.2 wt %), Cr from the tube material (4.7 wt %), Ni from the alloying elements in the tube material (1.6 wt %), and Ca and Cu (2.8 and 2.3 wt %, respectively). Ca and Cu most probably originate from the fuel additives. Metal-based additives are used as combustion catalysts to help the combustion and to reduce emissions and fuel consumption for hydrocarbon fuels. These metal-based additives include Mn, Ba, Ce, Pt, Fe, Cu, and Ca.[16,25−27] Furthermore, Ca is typically also found in antistatic additives.[17]

From the depth profiles (Figure 11), it is clear that the concentrations of C and O continuously decreased throughout the entire sputtering depth, while concentrations of Fe and Cr continuously increased. Obviously, the deposit layer was composed primarily of the main pyrolytic product C but contained also a significant amount of Fe from the tube material possibly originating from the steel wear particles embedded in the deposit layer. Other elements, which were present in relatively low concentrations, originate either from the pyrolytic process (O), the tube material (Cr and Ni) or the jet fuel (S), and the jet fuel additives (N, Al, P, Ca, and Cu).

2.2.3. Dark Area on the Inner Surface of Sample S2. Figure 12 shows the XPS spectra from the dark area on the inner surface of sample S2 before and after sputtering with Ar^+ ions for 6110 s, while in Table 5, the quantified values from these spectra are presented. Before sputtering, high concentrations of C and O (∼74 and 21 wt %, respectively) and low concentrations of N and Fe (∼2.6 and 2.5 wt %, respectively) were detected. After sputtering, to a depth of ∼300 nm, C and O concentrations decreased to 21 and 1.8 wt %, respectively; N concentration decreased to 0.8 wt %, while Fe concentration increased to 56 wt %. The following elements, which were not detected before sputtering, were additionally detected: Ar from sputtering with Ar^+ ions (1.9 wt %), Cr from the tube material (12.2 wt %), and Ti and Ni from the alloying elements in the tube material (1.4 and 4.8 wt %, respectively). It is interesting to note that no elements from the fuel additives, which were found in the deposit layer, were detected.

From the depth profiles (Figure 13), a gradual decrease of C and O concentrations and a simultaneous increase of Fe and

DOI: 10.1021/acsomega.8b03576
ACS Omega 2019, 4, 8255−8273

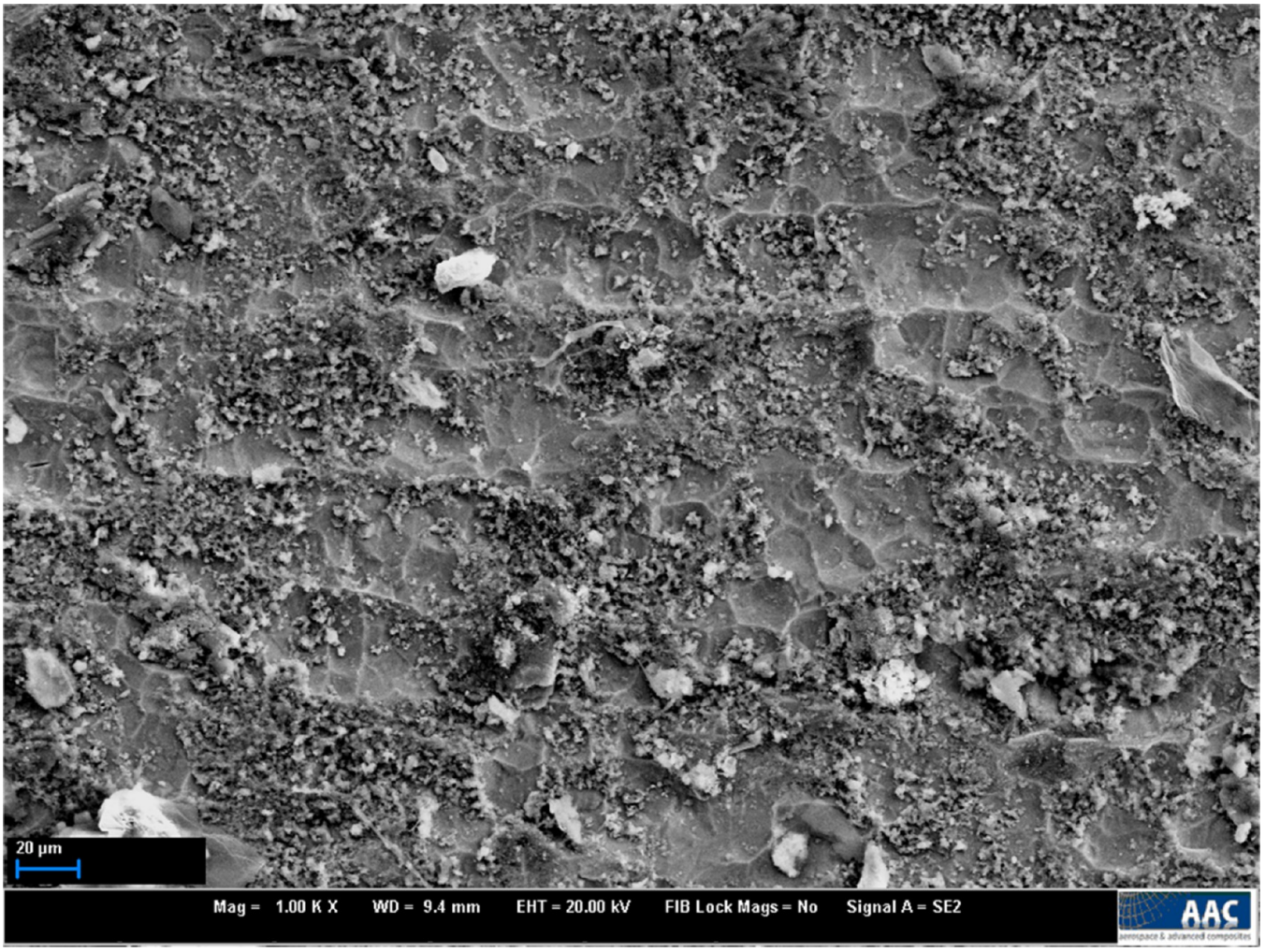

Figure 7. SEM image of the inner surface of the titanium sample.

Table 1. Elemental Concentrations from EDX Analyses on the Inner Surface of the Titanium Sample[a]

element	wt %
C	1.75 ± 0.91
O	24.43 ± 10.88
Na	0.23 ± 0.40
Mg	0.30 ± 0.32
Al	1.32 ± 1.16
Si	4.32 ± 2.78
P	0.39 ± 0.34
S	0.38 ± 0.44
K	0.37 ± 0.34
Ca	0.41 ± 0.43
Ti	64.83 ± 16.86
Fe	1.27 ± 1.12

[a]Average values and standard deviations from three measuring points are presented.

Cr concentrations could be observed throughout the entire sputtering depth of ∼300 nm. It is clear that at the final sputtering depth, the tube material had still not been reached (the C had a concentration of ∼21 wt %, while the Fe concentration was only ∼56 wt %). Thus, it could be concluded that due to the intergranular penetration, the steel surface was either chemically modified through C enrichment or patches of the deposit (with a thickness of more than 300 nm) remained anchored to the steel surface even after ultrasonic cleaning.

2.2.4. Bright Area on the Inner Surface of Sample S2. Figure 14 shows the XPS spectra from the bright area on the inner surface of sample S2 before and after sputtering with Ar^+ ions for 6110 s, and in Table 6, the quantified values from these spectra are presented. Before sputtering, the bright area showed a very similar composition to the dark area, while after sputtering to a depth of ∼300 nm, especially C and O concentrations were significantly lower as compared to those in the dark area (∼1.7 and 0.3 wt %, respectively). Correspondingly, Fe concentration was higher (∼70 wt %) as compared to the dark area (56 wt %).

From the depth profiles (Figure 15), it is clear that the tube material had already been reached at a depth of ∼100 nm as with a further increase in sputtering, the Fe, Cr, Ti, and Ni concentrations remained more or less constant, while the concentrations of C and O gradually approached zero (remains of elements due to the so-called "shading effect", see Section 2.2.1). This indicates that the chemically modified area was significantly thinner as compared to the dark area and had a depth of ∼100 nm.

2.2.5. Outer Surface of Sample T1. Figure 16 shows the XPS spectra from the outer surface of sample T1 before and after sputtering with Ar^+ ions for 9412 s, and in Table 7, the

DOI: 10.1021/acsomega.8b03576
ACS Omega 2019, 4, 8255−8273

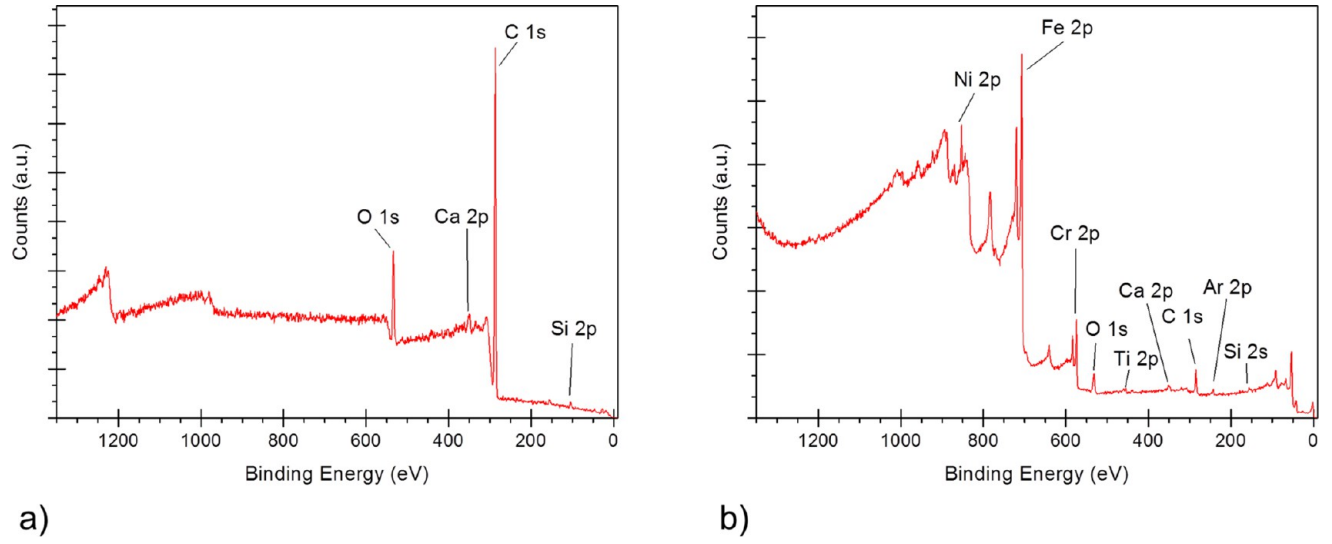

Figure 8. XPS spectra from the outer surface of sample S1 (a) before and (b) after sputtering with Ar^+ ions for 6110 s (sputtering depth of ~300 nm).

Table 2. Quantification of XPS Spectra from the Outer Surface of Sample S1 before and after Sputtering with Ar^+ Ions for 6110 s[a]

element	wt % before sputtering	wt % after sputtering
C	80.4	8.3
O	12.4	4.4
Si	4.0	2.5
Ar		1.4
Ca	3.4	1.4
Ti		1.3
Cr		12.9
Fe		60.1
Ni		7.6

[a]Deviations from 100% are due to rounding.

quantified values from these spectra are presented. Before sputtering, high concentrations of C and O (~60 and 25 wt %, respectively) and relatively low concentrations of N, Si, Na, and Ca (~4, 8, 1, and 3 wt %, respectively) were observed. It is interesting to note that Si and Ca were also detected on the outer surface of sample S1 (Table 2). Since according to the GOST 19807−91 standard (Table 10), OT4-1 titanium can contain up to 0.12 wt % Si, the detected Si could originate from the tube. On the other hand, the presence of N, Na, and Ca, which are typically present in jet fuel and oil additives,[16,17] confirms that the outer surface of the titanium tubes has been in contact with the surrounding engine oil used for cooling the tubes in the injection system.

After sputtering to a sputtering depth of ~470 nm, the C and O concentrations significantly decreased (to ~3 and 6 wt %, respectively), Si and Ca concentrations slightly decreased (to ~3.5 and 1.5 wt %, respectively), and N and Na were not detected anymore. At the same time, Ti, which was not detected before sputtering, had a very high concentration of ~81 wt %. After sputtering, the following elements, which also were not detected before sputtering, were additionally detected: Ar from sputtering with Ar^+ ions (~3 wt %) and Al (~2 wt %) possibly from the jet fuel and/or jet oil additives.

From the depth profiles (Figure 17), a gradual decrease of C, O, and Si and a simultaneous increase of Ti concentration can be observed. It is interesting to note that within the first 50 nm of sputtering depth, O, Na, Mg, Al, Si, Ca, and Fe concentrations initially increased and then started to decrease.

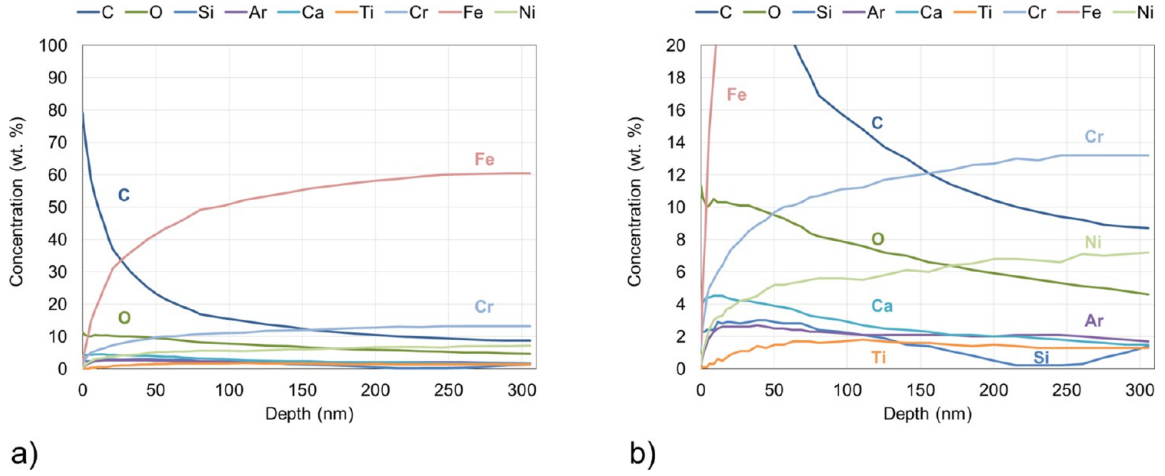

Figure 9. Depth profiles from the outer surface of sample S1. The *y* axis maximum is set at (a) 100 and (b) 20 wt %.

DOI: 10.1021/acsomega.8b03576
ACS Omega 2019, 4, 8255−8273

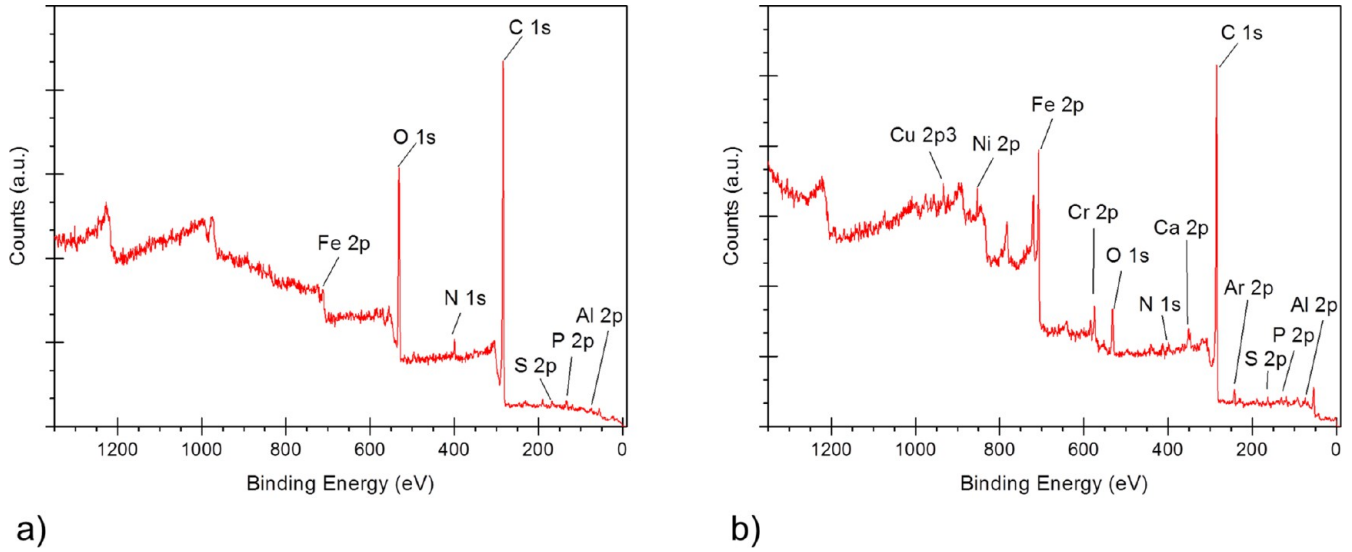

Figure 10. XPS spectra from the inner surface of sample S1 (a) before and (b) after sputtering with Ar^+ ions for 10610 s (sputtering depth of ∼530 nm).

Table 3. Quantification of XPS Spectra from the Inner Surface of Sample S1 before and after Sputtering with Ar^+ Ions for 10610 s[a]

element	wt % before sputtering	wt % after sputtering
C	65.6	51.8
N	1.7	0.5
O	17.1	4.9
Al	5.6	4.6
P	3.2	2.4
S	2.4	1.7
Ar		2.2
Ca		2.8
Cr		4.7
Fe	4.5	20.7
Ni		1.6
Cu		2.3

[a]Deviations from 100% are due to rounding.

Table 4. Detailed Composition of Chemical Species on the Inner Surface of Sample S1 before Sputtering Based on the Binding Energies (BE) from XPS Spectra

element	chemical bond	BE (eV)	wt %
Al	Al oxides	73.8	4.06
P	phosphates	132.44	3.28
C	C−C/carbidic C	283.57	31.28
	C−C/C−H	284.66	27.86
	C−O	287.68	3.62
N	organic bounded	399.33	2.90
O	metallic oxide	530.49	12.10
	organic/hydroxide	532.04	10.03
Fe	Fe	706.95	0.88
	FeOOH and III+	710.16 and 712.15	4.00

Na, Mg, and Fe were detected after the initial sputtering step of 10 s, and their concentrations decreased to zero at sputtering depths of ∼100, 420, and 280 nm, respectively. The maximum concentrations were 2, 3.1, and 5.5 wt % for Na, Mg, and Fe, respectively. It is interesting to note that Na and Mg were not detected on samples S1 and S2. Most probably, they originate from the lubricant additives in the surrounding engine oil since both are typically found in lubricant detergents,[28] while Na is found also in oil thickeners (soap-based) and soap-type greases.[29] According to the GOST 19807−91 standard, up to 0.3 wt % Fe can be found in OT4-1 titanium (Table 10). Most interesting are the distributions of C and O: Namely, the concentration of O throughout the entire sputtering depth is approximately twice that of C. Obviously, the composition of the deposition layer on the outer surface of the titanium tube was different from that observed on the stainless steel tube where the concentration of C was always higher than that of O. At the final sputtering depth of ∼470 nm, O and C concentrations were still relatively high (∼3 and 6 wt %, respectively) and still decreasing, while the Ti concentration was still increasing slightly, indicating that the unaffected base material had still not been reached.

2.2.6. Inner Surface of Sample T1. Figure 18 shows the XPS spectra from the inner surface of sample T1 before and after sputtering with Ar^+ ions for 20671 s, and in Table 8, the quantified values from these spectra are presented. Before sputtering, the C concentration was significantly lower than on the outer surface (27 wt %), while the O concentration was significantly higher (41 wt %). A relatively high concentration of Si (∼21 wt %) and low concentrations of Al (∼5 wt %), Ca (∼2 wt %), and Fe (∼2 wt %) were also detected. After sputtering to a sputtering depth of ∼1 μm, the O concentration slightly decreased but was still relatively high (∼17 wt %), while the C concentration significantly decreased (to ∼1 wt %). After sputtering, Ti, which was not detected before sputtering, was now present at ∼52 wt %. At the same time, Al concentration increased to ∼11 wt %, Si concentration decreased to ∼9 wt %, and Ca and Fe concentrations slightly increased to 3.5 and ∼4 wt %, respectively. After sputtering, the following elements, which were not detected before sputtering, were additionally detected: 1.8 wt % Ar from sputtering with Ar^+ ions and 0.4 wt % Mg.

From the depth profiles (Figure 19), it is clear that the concentrations of O, C, and Si were constantly decreasing throughout the entire sputtering depth, while the concentrations of Ti, Al, and Ar were constantly increasing. The concentrations of Mg, Fe, and Ca were more or less constant

DOI: 10.1021/acsomega.8b03576
ACS Omega 2019, 4, 8255−8273

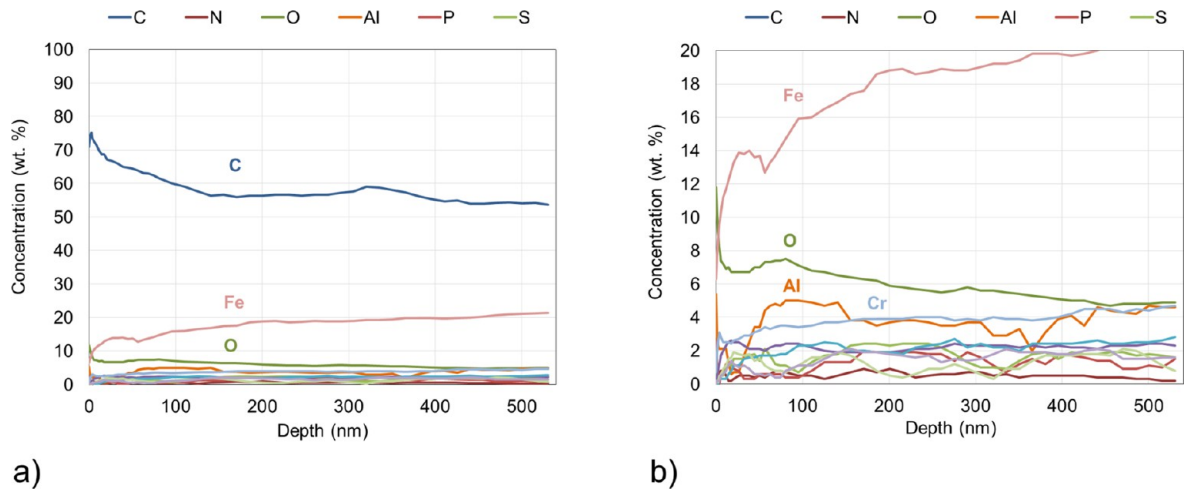

Figure 11. Depth profiles from the inner surface of sample S1. The *y* axis maximum is set at (a) 100 and (b) 20 wt %.

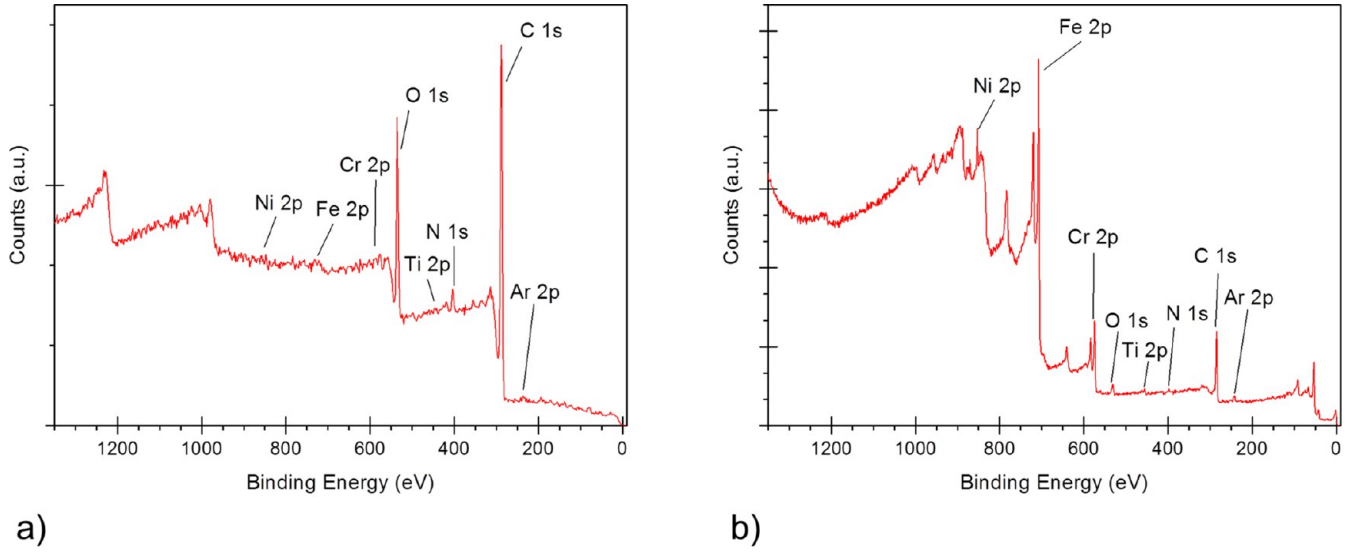

Figure 12. XPS spectra from the dark surface on the inner surface of sample S2 (a) before and (b) after sputtering with Ar^+ ions for 6110 s (sputtering depth of ~300 nm).

Table 5. Quantification of XPS Spectra from the Dark Area on the Inner Surface of Sample S2 before and after Sputtering with Ar^+ Ions for 6110 s

element	wt % before sputtering	wt % after sputtering
C	73.8	21.0
N	2.6	0.8
O	21.1	1.8
Ar		1.9
Ti		1.4
Cr		12.2
Fe	2.5	56.0
Ni		4.8

throughout the entire sputtering depth. At a sputtering depth of ~200 nm, the C concentration was already lower than 4 wt %, and it decreased at a slightly lower rate with further sputtering. This indicates that sputtering to a depth of ~200 nm removed most of the C-containing deposit layer from the surface.

It is interesting to note that Mg, which was not detected on samples S1 and S2, was detected on both the outer and the inner surface of sample T1. It has a more or less constant distribution throughout the entire sputtering depth on the inner surface, which indicates that Mg could originate from the tube material as an alloying element or an impurity considering that Mg is not specified for OT4-1 titanium by the GOST 19807−91 standard (Table 10). Also interesting is the presence of Fe, which increased with sputtering depth and was also detected on the outer surface of the sample indicating that Fe most likely is a constitutive element of the titanium tube material (Table 10).

Compared to the outer surface, on the inner surface of sample T1, significantly less C and more O were detected, which indicates that on the inner surface, oxidation was more pronounced than C deposit formation. Until a depth of ~200 nm, the C concentration was between 20 and 4 wt %; this indicates that a very thin pyrolytic deposition layer was present on the surface. Furthermore, since the O concentration remained almost constant throughout the entire sputtering depth of ~1 μm, this indicates that a relatively thick oxide layer had formed on the inner tube surface.

DOI: 10.1021/acsomega.8b03576
ACS Omega 2019, 4, 8255−8273

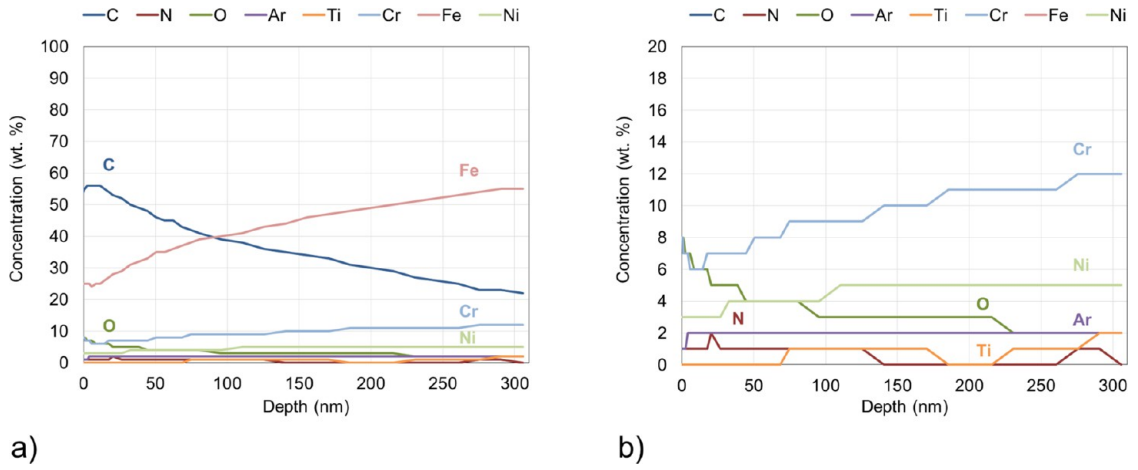

Figure 13. Depth profiles from the dark area on the inner surface of sample S2. The *y* axis maximum is set at (a) 100 and (b) 20 wt %.

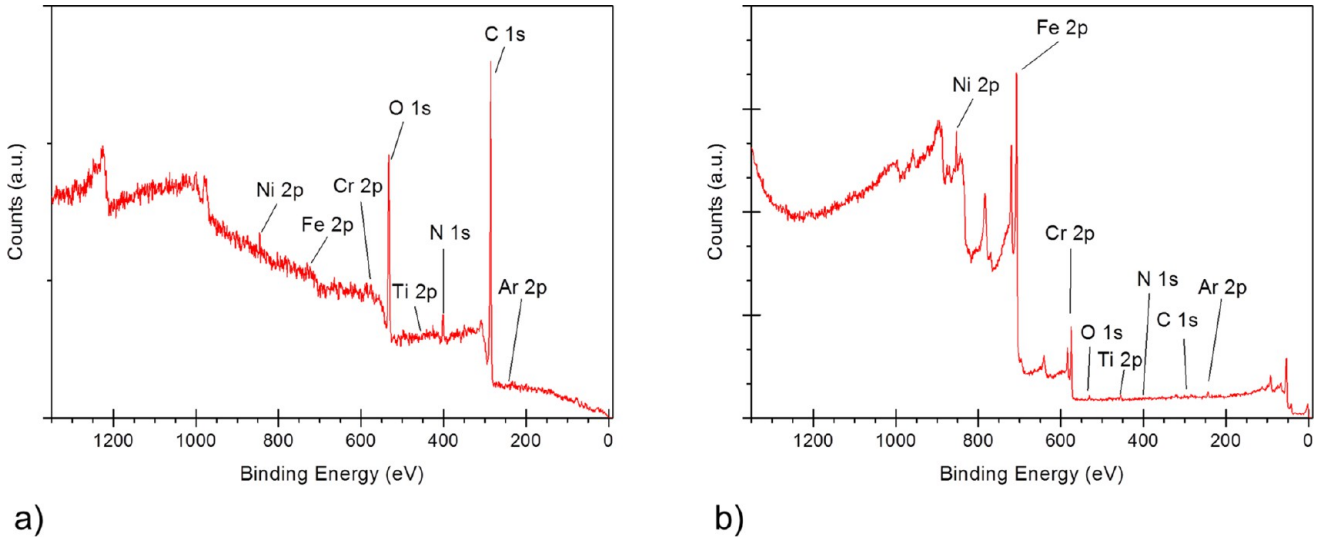

Figure 14. XPS spectra from the bright area on the inner surface of sample S2 (a) before and (b) after sputtering with Ar^+ ions for 6110 s (sputtering depth of ~300 nm).

Table 6. Quantification of XPS Spectra from the Bright Area on the Inner Surface of Sample S2 before and after Sputtering with Ar^+ Ions for 6110 s

element	wt % before sputtering	wt % after sputtering
C	69.4	1.7
N	5.0	0.4
O	23.4	0.3
Ar		2.2
Ti		1.7
Cr		14.8
Fe	2.3	70.4
Ni		8.4

Detailed analysis of the survey spectra at different sputtering depths showed that on the inner surface of the Ti tube, Ti oxides (TiO_2) were present in a relatively small amount and only within the first 100 nm of depth, while other oxides were present throughout the entire depth profile and consisted predominantly of Al and Si oxides. At a depth of ~50 nm, the ratio between the oxidized and the non-oxidized Ti was ~1:1 (binding energy for Ti is ~454 eV, while for TiO_2, it is >458 eV, which is well visible in the survey spectra), while after 100 nm, predominantly metallic Ti (Ti^0) was present. It should be noted that within the first 100 nm of depth, the maximum Ti concentration was ~15 wt %, which indicates that the amount of TiO_2 was relatively low. On the other hand, Al, Si, Ca, and Mg were fully oxidized throughout the entire depth profile. The Al peak showed no plasmon structure, which indicates that it was in an oxidized state (on a metallic Al peak, typically, a pronounced plasmon structure is observed). Al oxide was most probably present as Al_2O_3 since the binding energy of Al 2p was at ~76 eV. The Si peak showed no plasmon structure, which indicates that it was in an oxidized state. Si oxide was most probably present as SiO_2 since the binding energy of Si 2p was at ~104 eV. Ca and Mg did not show any pronounced shifts; however, they were oxidized as differential charging appeared (leading to shifted binding energy of ~354 eV for Ca 2p, normally visible at ~348 eV).

3. DISCUSSION

3.1. Stainless Steel Tube. By means of XPS, it has been possible to define very accurately the concentration of specific elements in the deposit layer on the bore of the tube and to attribute them to their most likely sources of origin. In Table 9,

DOI: 10.1021/acsomega.8b03576
ACS Omega 2019, 4, 8255−8273

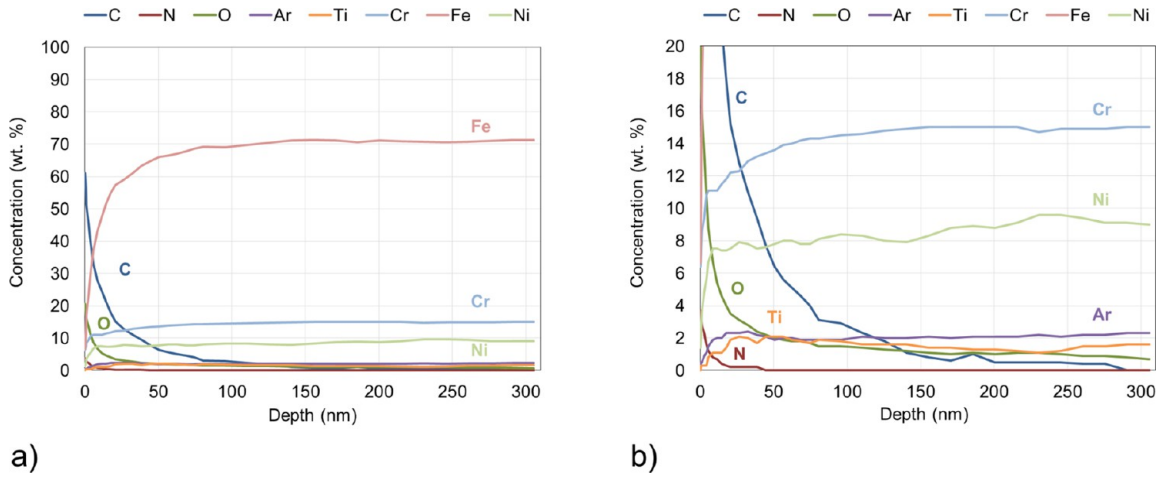

Figure 15. Depth profiles from the bright area on the inner surface of sample S2. The *y* axis maximum is set at (a) 100 and (b) 20 wt %.

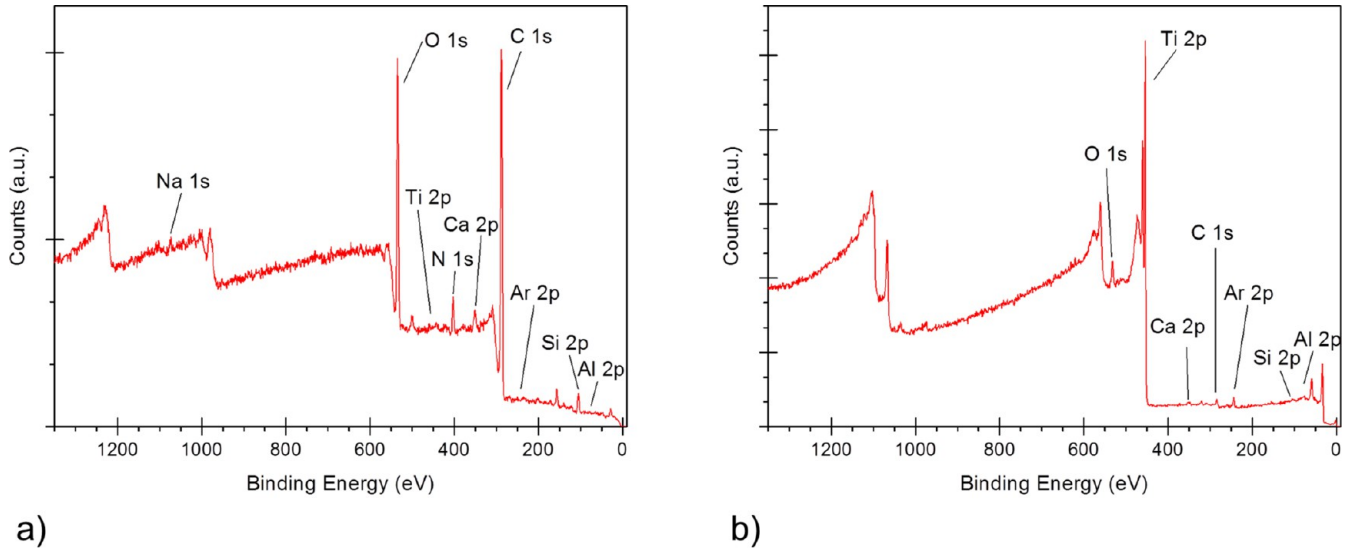

Figure 16. XPS spectra from the outer surface of sample T1 (a) before and (b) after sputtering with Ar^+ ions for 9412 s (sputtering depth of ~470 nm).

Table 7. Quantification of XPS Spectra from the Outer Surface of Sample T1 before and after Sputtering with Ar^+ Ions for 9412 s

element	wt % before sputtering	wt % after sputtering
C	59.4	3.1
N	4.2	0.0
O	25.0	6.0
Na	1.0	0.0
Al	0.0	1.9
Si	7.6	3.7
Ar	0.0	2.7
Ca	3.0	1.3
Ti	0.0	81.3

the chemical composition of the pyrolytic deposit layer on the bore of stainless steel tube is summarized together with the possible origins of each detected component. From Table 9, it can be concluded that the origin of the detected elements in the surface deposit can be attributed to (i) pyrolytic coke (C and O together accounting for 82.7 and 57.9 wt % before and after sputtering, respectively), (ii) tube material (Fe, Cr, and Ni together accounting for 4.5 and 27.6 wt % before and after sputtering, respectively), (iii) fuel (S with 2.4 and 1.7 wt % before and after sputtering, respectively) and (iv) fuel additives (N, Al, P, Ca, and Cu together accounting for 10.5 and 12.9 wt % before and after sputtering, respectively). From Table 9, it is clear that with increasing the sputtering depth, the concentration of pyrolytic products (C and O) decreased, while the concentrations of elements from the tube material (Fe, Cr, and Ni) increased. Some elements from the fuel (S) and the fuel additives (N, Al, and P) showed a slight decrease in concentration with sputtering depth, while with others (Ca and Cu), an increase in concentration was observed. However, it should be pointed out that the described changes in elemental concentrations occurred within the first 150 nm of sputtering depth, while afterward, the elemental concentrations remained more or less constant, as can be seen from Figure 11. This indicates that after 150 nm of sputtering depth, the deposit layer had a homogeneous chemical composition, which most probably did not significantly change throughout further thickness of the deposit.

After ultrasonically cleaning with distilled water, apart from N, no elements from the fuel or the fuel additives (S, Al, P, Ca,

DOI: 10.1021/acsomega.8b03576
ACS Omega 2019, 4, 8255−8273

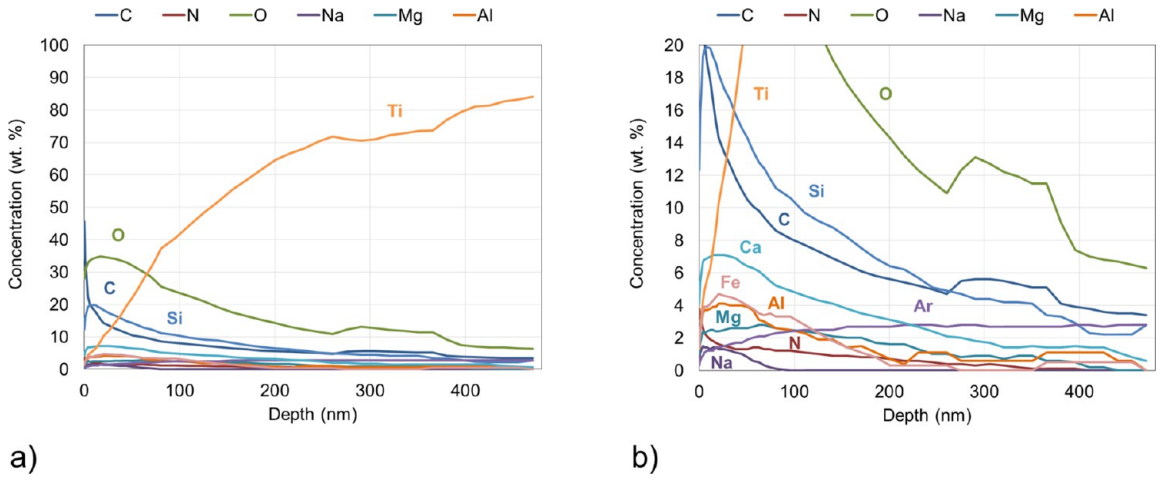

Figure 17. Depth profiles from the outer surface of sample T1. The *y* axis maximum is set at (a) 100 and (b) 20 wt %.

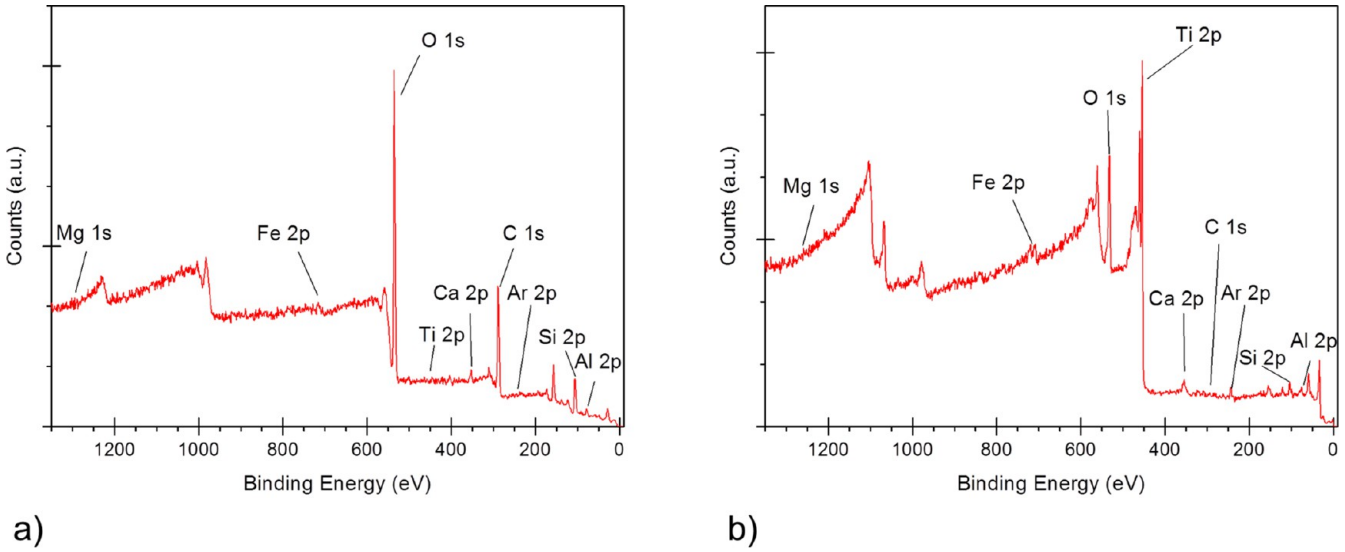

Figure 18. XPS spectra from the inner surface of sample T1 (a) before and (b) after sputtering with Ar^+ ions for 20671 s (sputtering depth of ~1030 nm).

Table 8. Quantification of XPS Spectra from the Inner Surface of Sample T1 before and after Sputtering with Ar^+ Ions for 20671 s

element	wt % before sputtering	wt % after sputtering
C	27.4	1.2
O	41.1	16.6
Mg		0.4
Al	5.4	11.0
Si	21.4	9.3
Ar		1.8
Ca	2.4	3.5
Ti		51.9
Fe	2.3	4.3

or Cu) were detected on the stainless steel surface (sample S2). This shows that these elements did not adsorb or diffuse into the tube material at a significant amount. However, on the dark area on sample S2, at a depth of 300 nm, the C concentration was still quite high (21 wt %), which shows that either the pyrolytic decomposition products have diffused into the base material and chemically modified it or that due to intergranular penetration, parts of the deposit have remained anchored to the steel surface even after ultrasonic cleaning.

It is interesting to note that the thickness of the C-rich layer on the bright area on the inner surface of sample S2 (~100 nm) was lower than on the outer surface of sample S1 (~200 nm), which is most probably because sample S2 was ultrasonically cleaned in distilled water. Furthermore, on the outer surface of sample S1, Si and Ca were detected, which were not found on the bright area on sample S2. This indicates that the deposition layer on the outer surface of sample S1 had a high thickness and was chemically complex. This layer was formed due to the interactions with the oil from the fuel-oil heat exchanger in contact with the outside of the tubes. Obviously, a bidirectional contamination occurs on the fuel tubes: from the inside to the core due to the jet fuel and from the outside to the core due to oil. On the other hand, on the bright area of sample S2, N was detected, which was not found on the outer surface of sample S1.

It is generally accepted that the formation of carbon deposits is mainly assigned to three paths: thermal oxidation, condensation of aromatic compounds, and metal catalytic coking, wherein metal catalytic coking is the main cause of the

DOI: 10.1021/acsomega.8b03576
ACS Omega 2019, 4, 8255−8273

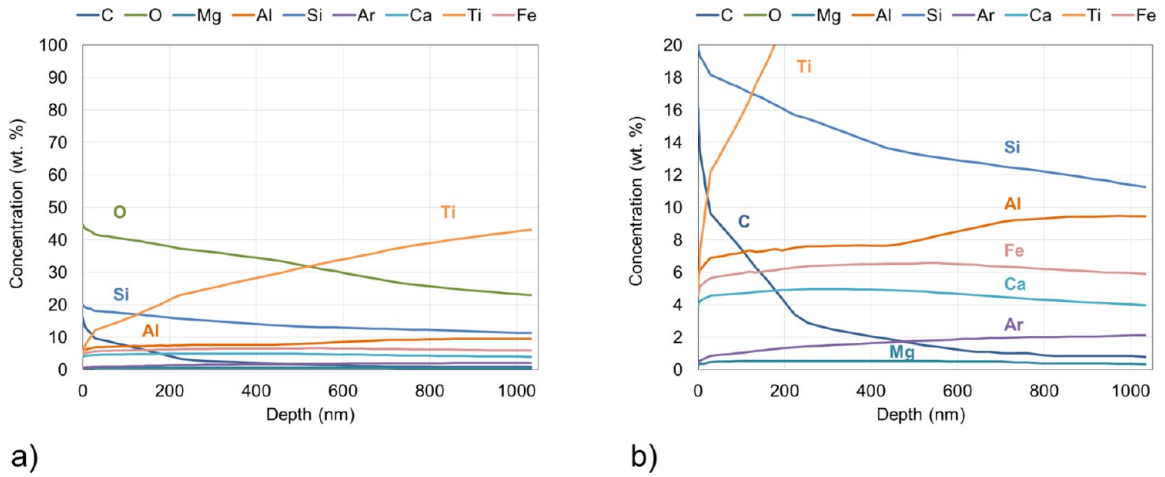

Figure 19. Depth profiles from the inner surface of sample T1. The *y* axis maximum is set at (a) 100 and (b) 20 wt %.

Table 9. Constitutive Chemical Elements of the Surface Deposit Layer on the Bore of Stainless Steel Tube and Their Origin[a]

origin	element	wt % before sputtering	wt % after sputtering	description
pyrolytic coke	C	65.6	52.9	C−C and carbidic C, organic aliphatic carbon of C−C or C−H-type, and C−O compounds
	O	17.1	5.0	C−O compounds
tube material	Fe	4.5	21.1	stainless steel
	Cr		4.8	stainless steel (alloying element)
	Ni		1.6	stainless steel (alloying element)
fuel	S	2.4	1.7	inevitable component present in all mineral oil products
fuel additives	N	1.7	0.5	present in deposit control additives (detergents), conductivity improvers (antistatic additives), H_2S "scavengers", combustion improvers and ignition improvers
	Al	5.6	4.7	present in the form of Al or Al_2O_3—possibly as nanoparticle additives for improvement of the ignition probability of jet fuel
	P	3.2	2.4	possibly anti-valve seat recession additives used to reduce the recession of exhaust valve seats in spark ignition engines
	Ca		2.9	metal-based additives used as combustion catalysts—Ca is typically also found in antistatic additives
	Cu		2.3	Metal-based additives used as combustion catalysts

[a]Weight concentrations after sputtering are recalculated by omitting Ar from the total summary of concentrations (100 wt % = without Ar).

large amount of surface deposits.[1,30] On stainless steel surfaces, deposition is typically initiated by chemical reactions of fuel species (particularly S species) and decomposition/dehydrogenation of hydrocarbons by transition-metal catalysis (e.g., of Fe and Ni)—this is known as filamentous carbon formation. These mechanisms are discussed in detail in the publications of Altin, Eser, and Venkataraman.[3,9−11]

The surface damage observed on the stainless steel surface after removal of deposits (Figure 6b) is consistent with metal (Fe and/or Ni) sulfide formation that would roughen the metal surface even at temperatures as low as 150 °C and activate the surface for catalytic deposition. In Figure 20, SEM images of the pyrolytic carbon deposit are shown. At lower magnifications, the deposit shows an amorphous structure (Figure 20a,b), as is typically found at these magnifications (5000:1 and 10,000:1).[31] However, at higher magnifications (20,000:1 and 50,000:1), a porous structure resembling filaments 100−200 nm in diameter, which have grown together, can be seen (Figure 20c,d). It is possible that subsequent pyrolytic deposition on incipient filaments may have obscured the observation of the original filaments underneath the pyrolytic deposit. A similar carbon deposit morphology was observed for pyrolytic ethylene, *n*-dodecane, and RP-2 fuel on a Cr−Zr copper alloy.[32]

Raman spectra on sample S1 (Figure 21) show similar characteristics as already observed in a study of structural and textural properties of catalytic filamentous carbon.[31] Bands at ∼1340 and 1580 cm^{-1} correspond to the so-called D and G modes of the carbon spectrum, respectively. The G mode is assigned to the in-plane displacement of carbon atoms in the hexagonal (graphite) sheets, while the D mode is related to the breathing modes of sp^2 atoms in rings and occurs when disorder is introduced into the graphite structure. The shoulder at 1615 cm^{-1} and a strong band at ∼2690 cm^{-1} could be correlated with the D′ and 2D mode of the carbon spectrum, respectively, both indicating a disordered nature of the graphitic structure. The band at ∼2690 cm^{-1} could alternatively be correlated to aldehydes, organic compounds containing a functional group with the structure −CHO, while the additional band at ∼680 cm^{-1} could be correlated to C−S bonds and/or C−C aliphatic chains.

The relative intensity ratio of the D band to the G band (I_D/I_G) can be used as an indication of the degree of graphitization of coke.[31,33] For sample S1, the value of I_D/I_G was 0.81 (<1), which indicates relatively low disorder of the graphitic structure. For filamentous coke synthesized under laboratory conditions on a 310S substrate, the value of I_D/I_G was significantly higher, 3.43, indicating higher disorder of the graphitic structure.[31]

DOI: 10.1021/acsomega.8b03576
ACS Omega 2019, 4, 8255−8273

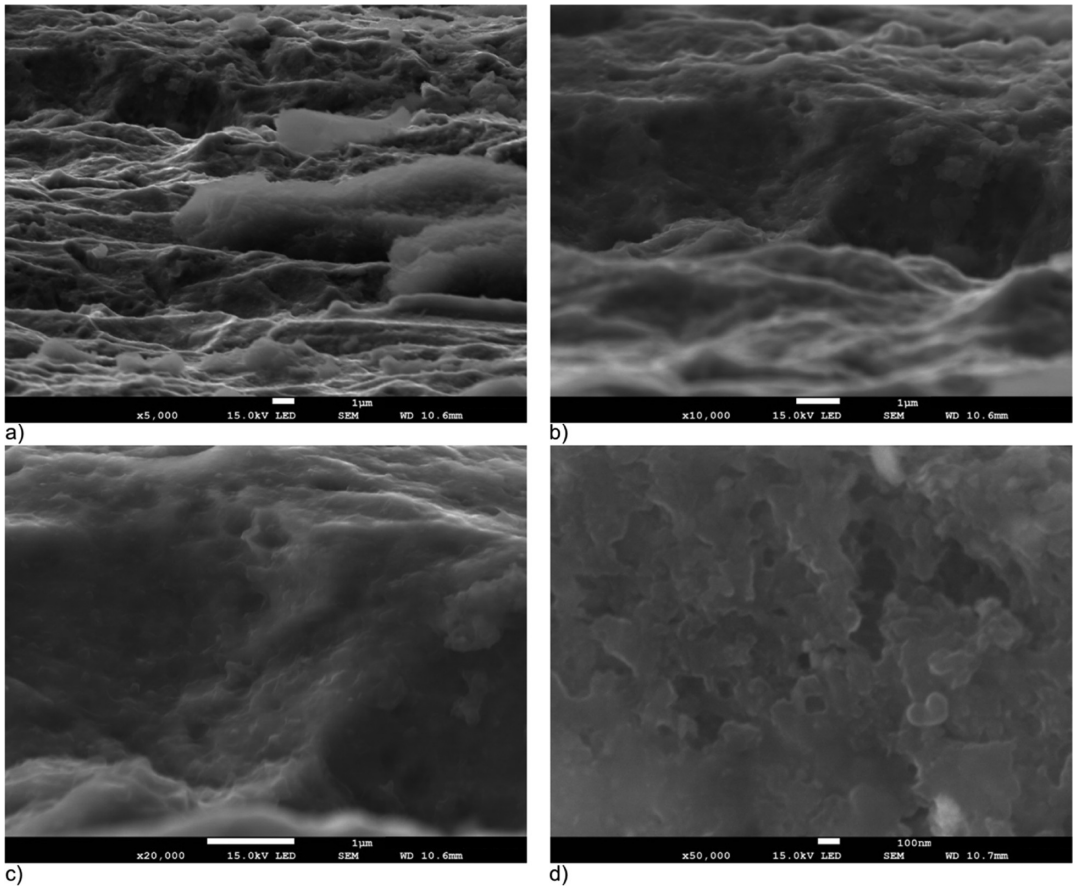

Figure 20. SEM micrographs of the deposit layer on the inner surface of sample S1 at different magnifications: (a) 5000:1, (b) 10,000:1, (c) 20,000:1, and (d) 50,000:1.

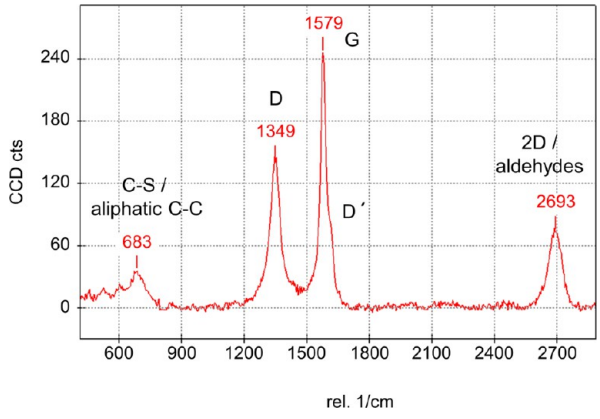

Figure 21. Typical Raman spectrum of the deposit layer on the inner surface of sample S1.

3.2. Titanium Tube. On the Ti tube, no surface deposits were observed; however, at high temperature and pressure (450 °C at 90 bar) due to the interactions with the subcritical kerosene, thermal oxidation at the titanium surface occurred. On the inner surface of sample T1, a very low C concentration was detected, indicating that the deposition rate of pyrolytic products from the fuel was significantly lower than on the stainless steel. At a sputtering depth of 200 nm, the C concentration had decreased to a value of ∼4 wt %, which indicates that the pyrolytic deposition layer was completely removed from the surface. The very high O concentration indicates that the surface was covered with an oxide layer thicker than 1 μm. The presence of Al and Ca indicates that diffusion of elements from the fuel additives into the tube material occurred.

In Figure 22, an estimated atomic distribution of the oxides on the inner side of the Ti tube—based on a detailed analysis of the survey spectra at different sputtering depths—is presented. The majority of the observed oxides are most probably products from the fuel oxidation that were deposited on and/or have diffused into the tube walls, while a small

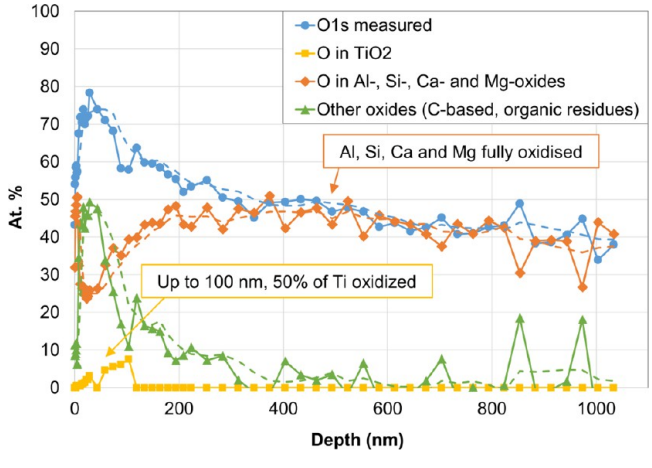

Figure 22. Estimated atomic distribution of oxides on the inner surface of sample T1.

DOI: 10.1021/acsomega.8b03576
ACS Omega 2019, 4, 8255−8273

amount could also represent the oxidized constitutive elements from the Ti tube. As the jet fuel is exposed to air, oxygen in air is dissolved in it. Accordingly, autoxidation reactions occur in the fuel temperature range of 150−400 °C.[34] The jet fuel reacts with dissolved oxygen to produce oxidized products, and deposits form on the inner wall surface. Various studies have already been performed on the thermal oxidation stability of jet fuels, where a short overview is provided in the work by Pei et al.[35] Although detailed elemental compositions of jet fuels are publicly unavailable, the oxide-forming elements, which were detected by XPS (Al, Si, Ca, and Mg), can be traced back to fuel additives as already described in Table 9. Additionally, it should be noted that Si and Al can enter the fuel during the manufacturing process (Al_2O_3 and SiO_2 are used as catalysts in the thermal cracking of kerosene[36]) or during engine operation in the form of chemical and/or mechanical wear particles. Zabarnick et al.[37] investigated the use of silylation additives for reducing oxidative deposition of jet fuels and reported that their disadvantage lies in the fact that silylating reagents and silylated products could be rapidly oxidized to SiO_2 within the combustion chamber. Furthermore, in characterization of jet aircraft engine particulates by XPS, Vander Wal and Byrg[38] showed that the presence and concentration of any particular elements appear to be very dependent upon the specific aircraft engine as well as its maintenance.

From EDX measurements on the cross section of sample T1 (Figure 23), the thickness of the oxide layer on the inner side

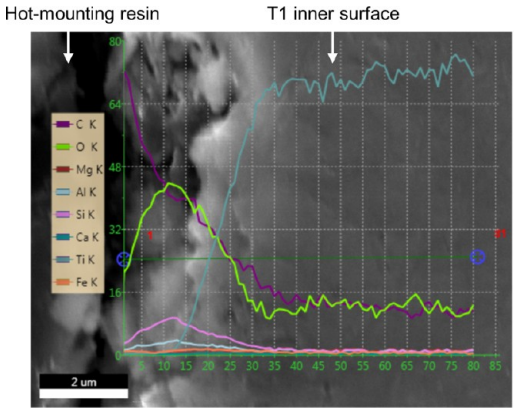

Figure 23. EDX elemental concentration depth profiles measured on the cross section of sample T1.

of the Ti tube can be estimated as ∼3 μm, the same depth to which the oxide building elements (Al, Si, Ca, and Mg) were detected. After ∼3 μm depth, their concentrations (it should be noted that predominantly, Al and Si were detected in higher concentrations) decreased to 0 atom %, and only Ti (from the tube material) and O (from the oxidation of the cross section in air) remained on the surface of the tube cross section. In the present study, on the cross-sectional surfaces of the Ti-tube, ∼20 atom % O was always detected due to oxidation of the nascent Ti surface.

Titanium has a particularly high reactivity, and therefore a short contact with the environment results in a passive oxide layer only a few nanometers thick.[39,40] The spontaneously forming passive layer is compact and morphologically uniform, has good adhesion to the substrate, and gives titanium excellent corrosion resistance and also ensures the chemical inertness of titanium in many environments. The corrosion resistance of titanium is strictly related to the quality of the protective passive layer, consisting mainly of titanium dioxide TiO_2.[41] This layer consists of an internal and an external part. The internal part consists of nonstoichiometric oxides, and the external part consists of amorphous TiO_2.[42] Due to the above described mechanisms, it is obvious that the original Ti tube was covered with a layer of TiO_2, which was (in combination with the underlying Ti) most probably responsible for the reduced pyrolytic coke deposition as compared to stainless steel. It is however not clear why on the inner surface of the Ti tube, only a very small amount of TiO_2 has remained. Possibly, this was largely removed during kerosene transport or replaced by other oxides, which have eventually deposited on the surfaces.

Using inert coatings, including Ti and Al oxides, for the reduction of carbon deposition from the cracking of fuels is a widely applied method. Altin et al.[43] have reported that ∼1 μm of Al and Ti oxide coatings on Inconel 718 coupons reduced carbon deposition by eliminating the catalytic activity of the metal alloy surface. Yang et al.[44] reported that the anticoking performance increased from 37 to 69% as the thickness of the Al_2O_3 coatings changed from 318 to 1280 nm. Tang et al.[31] reported that the inhibition effect of the TiN coating on coke growth is superior to that of other coatings such as Al_2O_3. The authors attribute this to the fact that the TiN coating not only creates a barrier between the hydrocarbon fuels and metal surface to inhibit related catalytic coke formation but also minimizes C deposits by absorbing C atoms.

4. SUMMARY

From the structural and chemical analyses of the stainless steel and titanium tube samples obtained from a turbofan engine after the end of its lifetime, the following conclusions on the pyrolytic deposition and its effects on the analyzed material samples can be drawn:

1 On the inner stainless steel tube surfaces, a carbon-based pyrolytic layer having a thickness of between 4 and 17 μm (average thickness of ∼9 μm) was observed. It was composed primarily of C and O; however, other elements such as N, Al, P, S, Ca, Cr, Fe, Ni, and Cu were also present in low quantities.

2 After the removal of the pyrolytic deposit layer on the bore of the tube, corrosion pits with a depth of 3−4 μm were identified in the contaminated area, and the surface roughness of the degraded surfaces was more than 2 times higher than that of the exterior surface of the tube. The fuel deposit had penetrated the tube surface intergranularly to a depth of ∼10 μm.

3 The origin of elements detected in the deposit layer on the inner surface of the stainless steel tube can be attributed to (i) pyrolytic coke (C and O together accounting for 82.7 and 57.9 wt % before and after sputtering, respectively), (ii) tube material (Fe, Cr, and Ni together accounting for 4.5 and 27.6 wt % before and after sputtering, respectively), (iii) fuel (S with 2.4 and 1.7 wt % before and after sputtering, respectively), and (iv) fuel additives (N, Al, P, Ca, and Cu together accounting for 10.5 and 12.9 wt % before and after sputtering, respectively).

4 After ultrasonically cleaning the stainless steel surface, apart from N, no elements from the fuel or the fuel additives (S, Al, P, Ca, or Cu) were detected, which

DOI: 10.1021/acsomega.8b03576
ACS Omega 2019, 4, 8255−8273

shows that these elements did not adsorb or diffuse into the base material. However, the surface was covered with dark patches with a high C concentration and a thickness of more than 300 nm, showing that either the pyrolytic decomposition products have diffused into the base material and chemically modified it or that due to intergranular penetration parts of the deposit have remained anchored to the steel surface even after ultrasonic cleaning.

5 On the inner surface of the titanium tube, the thickness of the C-rich fuel deposition layer was significantly thinner (~200 nm) as compared to the stainless steel surface (~9 μm). However, the surface was covered with an ~3 μm-thick layer of oxides containing elements from the fuel additives, which were identified as Al, Si, Ca, and Mg oxides.

6 It is believed that the beneficial properties of Ti covered with a thin layer of TiO_2, such as low adhesion and/or surface energy, have promoted different deposition mechanisms compared to stainless steel and thus prevented pyrolytic coke deposition and the related material deterioration observed on the stainless steel.

5. EXPERIMENTAL SECTION

5.1. Fuel Tubes and Sample Preparation. For the present investigation, two types of fuel tubes were analyzed: AISI 321 austenitic stainless steel fuel tube and OT4-1 titanium (Russian standard GOST 19807−91) equivalent to the Grade 4 unalloyed titanium 80 A. In Table 10, the chemical composition of both materials according to SAE international and GOST 19807−91 standards is presented.

Table 10. Standard-Specified Values for AISI 321 Stainless Steel (SAE International) and OT4−1 Titanium (GOST 19807−91)[a]

	standard	
element	AISI 321 stainless steel (SAE International) (wt %)	OT4-1 (GOST 19807−91) (wt %)
H	N/A	≤0.012
C	<0.12	≤0.1
N	N/A	≤0.05
O	N/A	≤ 0.15
Al	N/A	1.5−2.5
Si	<0.8	≤0.12
P	<0.035	N/A
S	<0.02	N/A
Ti	0.4−1	94.33−97.5
V	N/A	N/A
Cr	17−19	N/A
Mn	<2	0.7−2
Fe	~67	≤0.3
Co	N/A	N/A
Ni	9−11	N/A
Cu	<0.3	≤0.3
Zr	N/A	N/A
Nb	N/A	N/A
Mo	N/A	N/A
W	N/A	N/A
impurities	N/A	≤0.3

[a]N/A stands for "not available".

Both tube samples were collected from an Ivchenko AI-25 twin-shaft medium bypass turbofan engine after the end of its service life, that is, after the engine reached its cycle limit. The tubes were used in the same engine but in different parts of the fuel circuit. The stainless steel tube was part of the fuel-oil heat exchanger circuit used to cool the oil to temperatures below 150 °C at a maximum of 64 bar, while the titanium tube was used in the injection system where the temperature can reach 450 °C at a maximum of 90 bar. Since the titanium tube was connected to the fuel injector, its diameter was smaller than that of the stainless steel tube. The external diameters of the stainless steel and titanium tube were 16 and 8 mm, respectively.

In the engine, T-1 and TS-1 jet fuels were used. TS-1 is the main jet fuel grade available in Russian and CIS states. It is a kerosene-type fuel with slightly higher volatility (flash point is 28 °C minimum) and lower freeze point (<−50 °C) compared to Jet A-1 fuel. The exact chemical composition of the fuels used is not known since it can vary slightly depending on the manufacturer. The Russian standard GOST 10227−86 (Table 11) only specifies the components that affect fuel performance.

Table 11. T-1 Jet Fuel (First Grade OKP 02 5121 0202) Specifications According to GOST 10227−86 Standard

parameter	value
density at 20 °C, kg/m^3, at least	800
kinematic viscosity, mm^2/s (cSt)	
at 20 °C, not less than	1.5
at −40 °C, not more than	16
lower calorific value, kJ/kg, not less than	42,900
height of the smoke point, mm, not less than	20
acidity, mg KOH per 100 cm^3 of fuel, not more than	0.7
iodine number, 100 g of iodine per g of fuel, not more than	2
flash point in closed crucible (°C), not lower	30
onset of crystallization temperature (°C), max	60
thermal stability under static conditions at 150 °C, not more than	
sludge concentration in mg per 100 cm^3 of fuel	35
mass fraction of aromatic hydrocarbons (%), not more than	20
actual resin concentration in mg per 100 cm^3 of fuel, not more than	6
mass fraction of total sulfur (%), not more than	0.1
mass fraction of mercaptan sulfur (%), not more than	
mass fraction of hydrogen sulfide	absent
ash content (%), not more than	0.003
content of water-soluble acids and alkalis	absent
content of naphthenic acid soaps	absent
content of mechanical impurities and water	absent
mass fraction of naphthalene hydrocarbons (%), not more	

The maximum working fuel pressure was 90 bar, that is, above the supercritical pressure of the fuel, and the maximum exhaust gas temperature was 1198 °C, which was maintained with the help of air-fuel and oil-fuel coolers.

Samples for the analyses were cut from the stainless steel and titanium aviation tubes in the form of 10 to 20 mm-long tubular segments that were longitudinally cut into half-tubular, that is, U-shaped segments. Since the tubes were seamless, manufactured by cold drawing, it was assumed that the topographical properties were initially the same on the internal and the external tube walls. The outer surface of the stainless steel tube was in contact with the oil from the fuel-oil heat exchanger, while the outer surface of the titanium tubes was in

DOI: 10.1021/acsomega.8b03576
ACS Omega 2019, 4, 8255−8273

contact with the surrounding engine oil used for cooling the tubes. On the inner side of the stainless steel tubes, a thick black layer of jet fuel deposit was observed, while on titanium tubes, no visible deposit from the fuel was present. Therefore, titanium samples were analyzed only in their as-received state, while stainless steel samples were analyzed in their as-received state, that is, covered with the surface deposit layer, and after the removal of the deposited layers by ultrasonically cleaning in distilled water. In Figure 24, the analyzed samples S1, S2, and T1 are shown. Samples S1 and S2 were cut from the stainless steel tube, and sample T1 was cut from the titanium tube. Samples S1 (Figure 24a) and T1 (Figure 24c) were analyzed in their as-received state, while sample S2 (Figure 24b) was ultrasonically cleaned in distilled water. After ultrasonic cleaning, two distinct areas could be observed on the inner surface of sample S2: (i) bright regions where the deposited layer had most probably been fully removed and (ii) dark regions/patches where possibly the deposit had not fully detached from the surface; that is, it remained partially adhered to the surface, or the material surface had been chemically modified due to the diffusion of species from the deposit.

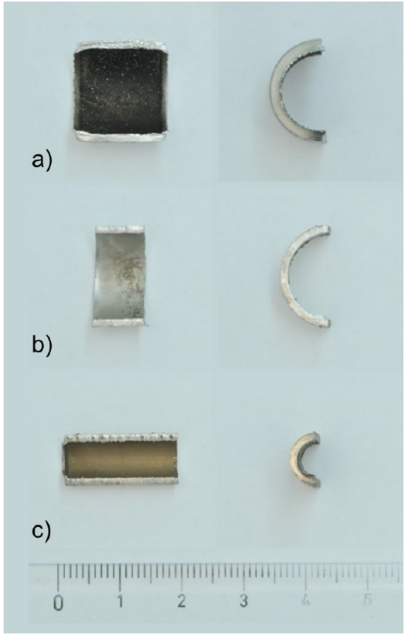

Figure 24. Inner surfaces and side views of the tube samples: (a) sample S1, the as-received stainless steel sample covered with a thick black layer of deposits from the jet fuel; (b) sample S2, the stainless steel sample ultrasonically cleaned in distilled water; and (c) sample T1, the as-received titanium sample.

For surface characterization and metallographic analyses, tube sections were prepared by hot mounting using an Opal 410 mounting process (ATM GmbH, Germany). Both longitudinal and transverse tube sections were metallographically prepared. In order to avoid melting of the deposited layer on the inner surface of the as-received stainless steel sample, these samples were cold mounted in resin. Polishing of the resin-embedded samples having a diameter of 30 mm was performed on a Struers Tegrapol-15 polishing machine (Struers ApS, Denmark). For grinding, Struers SiC grinding paper with grades from 120 to 1200 was used. Polishing was done mechanically on velvet-coated disks using 6 and 1 μm diamond pastes.

To reveal the microstructure of the samples, the resin-embedded sample cross sections were electrolytically etched in 10% oxalic acid solution at 12 V for 60 s.

5.2. Structural and Chemical Analyses. The microstructure of the sample cross sections and the deposit layer thickness were investigated by using an Olympus BX 51 polarized light microscope (Olympus Co., Japan).

On the cross section of the stainless steel samples, microhardness measurements were performed in order to evaluate the influence of surface deposits on the mechanical properties of the tube material. Measurements were carried out along the tube wall in longitudinal and perpendicular directions—from the outer to the inner surface of the tubes. Vickers hardness was measured by using a Matsuzawa MHT-1 microhardness tester calibrated with a test block at 211.6 HV1 according to EP14173575. On each sample, a force of 500/1000 gf was applied for 15 s. The diagonals of the indents were measured by using the Olympus BX 51 polarized light microscope.

Roughness parameters of the samples were acquired on the inner and outer tube surfaces by using a Taylor-Hobson Talysurf 120 L profilometer (AMETEK Taylor Hobson, UK). For detailed surface characterization, scanning electron microscopy (SEM) and energy-dispersive X-ray spectroscopy (EDX) analyses were performed with a Vega LMH II scanning electron microscope (TESCAN Brno, s.r.o., Czech Republic), a QuantaTM 450 FEG-SEM (Thermo Fisher Scientific, USA), a Supra VP40 high resolution scanning electron microscope (Carl Zeiss Microscopy GmbH, Germany), and a JSM-7100F field emission scanning electron microscope (JEOL Ltd., Japan).

For a detailed chemical analysis of the deposited layer and the contaminated surfaces, X-ray photoelectron spectroscopy (XPS) analyses were performed. XPS analyses were carried out with a Theta Probe (Thermo Fisher Scientific, East Grinstead, UK) equipped with a monochromatic Al Kα X-ray source ($h\nu$ = 1486.6 eV) and an Ar^+ ion gun. During the measurements, the base pressure in the analysis chamber was constantly in the low 10^{-7} Pa range.

Initially, for every measuring location, a survey scan was performed with a pass energy of 200 eV, and the resolution of the measurement spot was 400 μm. Afterward, depth profiles of the respective surfaces were acquired by sequentially measuring and sputtering the surface. After each sputtering step, the composition of the surface was determined from a survey scan. The area sputtered was 2 mm × 2 mm, with a sputter current of 1 μA at 3 kV. These parameters resulted in an estimated sputter yield of ~0.05 nm/s. In Table 12, sputtering times and sputtering depths, that is, the approximate depths of material removed, during the XPS analyses of the

Table 12. Sputtering Times and Sputtering Depths (Approximate Depths of Material Removed) during the XPS Analyses of the Tube Samples

sample	position	sputtering time (s)	sputtering depth (nm)
S1	outer surface	6110 (102 min)	300
	inner surface (deposit)	10610 (177 min)	530
S2	bright area	6110 (102 min)	300
	dark area	6110 (102 min)	300
T1	outer surface	9412 (157 min)	470
	inner surface	20671 (345 min)	1000

DOI: 10.1021/acsomega.8b03576
ACS Omega 2019, 4, 8255−8273

tube samples are listed. The outer surface of sample S1 and both positions of interest on sample S2 (bright and dark areas on the inner surface of the tube) were sputtered for 6110 s (102 min), which corresponds to ∼300 nm of sputtering depth. The inner surface of sample S1 was sputtered for 10610 s (177 min), which corresponds to ∼530 nm of sputtering depth. The outer surface of sample T1 was sputtered for 9412 s (157 min), which corresponds to ∼470 nm of sputtering depth, while the inner surface of sample T1 was sputtered for 20671 s (345 min), which corresponds to ∼1000 nm of sputtering depth. Thirty-five to fifty sputtering steps were applied by using increasing sputtering times of 10 to 600 s. The sputtering times were sequentially increased and were shorter at lower sputtering depths, being increased at higher sputtering depths.

All acquired XPS spectra were processed with the software package Avantage version 5.945 (Thermo Fisher Scientific, East Grinstead, UK) using Gaussian/ Lorentzian peak fitting for the narrow (high resolution) scans. The elemental analysis signal-to-noise threshold was set to 1.5 and a moving average was used for smoothing the depth profile curves.

Raman spectra of the deposit on sample S1 were acquired using an alpha 300R confocal Raman microscope (WITec GmbH, Germany) with 532 nm radiation from a Nd:YAG laser as the excitation source. The system was operated with an output power of 25 mW and a focal spot of the order of a few micrometers (1−2 μm^2). The back-scattered Raman signals in the region from 100 to 4000 cm^{-1} were collected and recorded.

AUTHOR INFORMATION

Corresponding Author

*E-mail: igor.velkavrh@v-research.at. Phone: +43 5572 394 159 28.

ORCID

Igor Velkavrh: 0000-0002-4293-9978

Present Address

†Metadynea Austria GmbH, Hafenstrasse 77, 3500 Krems, Austria.

Author Contributions

The manuscript was written through contributions of all authors. Regarding the experimental work, I.P. acquired the aviation tube samples and performed optical microscopy, SEM/EDX, and hardness and surface topography measurements on the steel tubes under the supervision of D.G.G., B.M., and M.R. J.B. and C.G. conducted XPS measurements on steel and titanium tubes and SEM/EDX measurements on titanium tubes. I.V. performed SEM/EDX and Raman measurements and conducted comparative analyses of all results under the supervision of A.D.. All authors have given approval to the final version of the manuscript.

Notes

The authors declare no competing financial interest.

ACKNOWLEDGMENTS

This work was funded by the Austrian COMET Programme (Project XTribology, no. 849109) and carried out at the "Excellence Centre of Tribology" (AC2T research GmbH) in cooperation with V-Research GmbH, University of Southampton and George Asachi Technical University of Iaşi.

REFERENCES

(1) Edwards, T.; Zabarnick, S. Supercritical fuel deposition mechanisms. *Ind. Eng. Chem. Res.* **1993**, *32*, 3117−3122.

(2) Towfighi, J.; Sadrameli, M.; Niaei, A. Coke Formation Mechanisms and Coke Inhibiting Methods in Pyrolysis Furnaces. *J. Chem. Eng. Jpn.* **2002**, *35*, 923−937.

(3) Altin, O.; Eser, S. Carbon deposit formation from thermal stressing of petroleum fuels. *Prepr. Pap. - Am. Chem. Soc., Div. Fuel Chem.* **2004**, *49*, 764−766.

(4) Mohan, A. R.; Eser, S. Analysis of carbonaceous solid deposits from thermal oxidative stressing of Jet-A fuel on Iron- and nickel-based alloy surfaces. *Ind. Eng. Chem. Res.* **2010**, *49*, 2722−2730.

(5) Albright, L. F.; Marek, J. C. Mechanistic model for formation of coke in pyrolysis units producing ethylene. *Ind. Eng. Chem. Res.* **1988**, *27*, 755−759.

(6) Balster, W. J.; Jones, E. G. Effects of temperature on formation of insolubles in aviation fuels. In *ASME 1997 International Gas Turbine and Aeroengine Congress and Exhibition Volume 2: Coal, Biomass and Alternative Fuels; Combustion and Fuels; Oil and Gas Applications; Cycle Innovations*; The American Society of Mechanical Engineers: New York, 1997; pp. V002T06A028−V002T06A028.

(7) DeWitt, M. J.; Edwards, T.; Shafer, L.; Brooks, D.; Striebich, R.; Bagley, S. P.; Wornat, M. J. Effect of Aviation Fuel Type on Pyrolytic Reactivity and Deposition Propensity under Supercritical Conditions. *Ind. Eng. Chem. Res.* **2011**, *50*, 10434−10451.

(8) Reyniers, M.-F. S. G.; Froment, G. F. Influence of metal surface and sulfur addition on coke deposition in the thermal cracking of hydrocarbons. *Ind. Eng. Chem. Res.* **1995**, *34*, 773−785.

(9) Venkataraman, R.; Eser, S. Characterization of Solid Deposits Formed from Short Durations of Jet Fuel Degradation: Carbonaceous Solids. *Ind. Eng. Chem. Res.* **2008**, *47*, 9337−9350.

(10) Venkataraman, R.; Eser, S. Characterization of Solid Deposits Formed from Jet Fuel Degradation under Pyrolytic Conditions: Metal Sulfides. *Ind. Eng. Chem. Res.* **2008**, *47*, 9351−9360.

(11) Eser, S.; Venkataraman, R.; Altin, O. Deposition of Carbonaceous Solids on Different Substrates from Thermal Stressing of JP-8 and Jet A Fuels. *Ind. Eng. Chem. Res.* **2006**, *45*, 8946−8955.

(12) Tan, C. D.; Baker, R. T. K. The effect of various sulfides on carbon deposition on nickel−iron particles. *Catal. Today* **2000**, *63*, 3−20.

(13) Altin, O.; Eser, S. Analysis of Solid Deposits from Thermal Stressing of a JP-8 Fuel on Different Tube Surfaces in a Flow Reactor. *Ind. Eng. Chem. Res.* **2001**, *40*, 596−603.

(14) López León, L. D.; Olguín Coca, F. J.; López León, A. L.; Márquez Casasola, M.; Baltazar Zamora, M. A.; Santiago Hurtado, G.; Volpi León, V. Corrosion of Carbon Steel in a Synthetic Environment and Kerosene on a System with Continuous Flow. *Int. J. Electrochem. Sci.* **2015**, *10*, 7582−7595.

(15) López León, L. D.; Veloz Rodríguez, M. A.; Reyes Cruz, V. E.; Pérez García, S. A.; Olguín Coca, F. J. Behaviour of Carbon Steel in the Presence of Hydrocarbon and a Pyridinic Compound. *Int. J. Electrochem. Sci.* **2014**, *9*, 1488−1496.

(16) Technical Committee of Petroleum Additive Manufacturers in Europe. *Fuel Additives: Use and Benefits*; ATC Document 113; 2013; pp. 23−56.

(17) Groysman, A. Fuel Additives. In *Corrosion in Systems for Storage and Transportation of Petroleum Products and Biofuels*; Springer Netherlands: Dordrecht, 2014; pp. 23−41.

(18) Guerieri, P. M.; DeLisio, J. B.; Zachariah, M. R. Nano-aluminum/Nitrocellulose microparticle additive for burn enhancement of liquid fuels. *Combust. Flame* **2017**, *176*, 220−228.

(19) Tyagi, H.; Phelan, P. E.; Prasher, R.; Peck, R.; Lee, T.; Pacheco, J. R.; Arentzen, P. Increased Hot-Plate Ignition Probability for Nanoparticle-Laden Diesel Fuel. *Nano Lett.* **2008**, *8*, 1410−1416.

(20) Karthikeyan, S.; Elango, A.; Silaimani, S. N.; Prathima, A. Role of Al_2O_3 nano additive in GSO Biodiesel on the working characteristics of a CI engine. *Indian J. Chem. Technol.* **2014**, *21*, 285−289.

DOI: 10.1021/acsomega.8b03576
ACS Omega 2019, 4, 8255−8273

(21) Waters, C. E. *Sulphur in petroleum oils. Technologic Papers of the Bureau of Standards*; Washington Government Printing Office: Washington, D.C., 1920.
(22) Santelli, R. E.; Oliveira, E. P.; de Carvalho, M. D. F. B.; Bezerra, M. A.; Freire, A. S. Total sulfur determination in gasoline, kerosene and diesel fuel using inductively coupled plasma optical emission spectrometry after direct sample introduction as detergent emulsions. *Spectrochim. Acta B* **2008**, *63*, 800−804.
(23) Yin, C.; Xia, D. A study of the distribution of sulfur compounds in gasoline produced in China. Part 1. A method for the determination of the distribution of sulfur compounds in light petroleum fractions and gasoline. *Fuel* **2001**, *80*, 607−610.
(24) Young, D. J. Corrosion by Sulphur. In *High Temperature Oxidation and Corrosion of Metals*; Elsevier Science: Amsterdam, Netherlands, 2016; pp. 393−430.
(25) May, W. R.; Hirs, E. A. Catalyst for Improving the Combustion Efficiency of Petroleum Fuels in Diesel Engines. *Presented at the 11th Diesel Engine Emissions Reduction Conference*, Chicago, IL, 2005; 16 pages.
(26) Kumar, M. V.; Babu, A. V.; Kumar, P. R. The impacts on combustion, performance and emissions of biodiesel by using additives in direct injection diesel engine. *Alexandria Eng. J.* **2018**, *57*, 509−516.
(27) Vasquez, J. M. G. Fuel additive. U.S. Patent US 20,130,283,674 A1, October 31, 2012.
(28) Rizvi, S. Q. A., Detergents. In *Lubricant Additives - Chemistry and Applications*, Second Edition; Rudnick, L. R., Ed.; CRC Press, Taylor & Francis Group: Boca Raton, FL, 2009; pp. 123−141.
(29) Ruge, I. W. Lubricating greases − characteristics and selection. In *CRC handbook of lubrication: theory and practice of tribology. Vol. 2: Theory and design*; Booser, E. R., Ed.; CRC Press: Boca Raton, FL, 1983; pp. 255−267.
(30) Albright, L. F.; Marek, J. C. Coke Formation during Pyrolysis: Roles of Residence Time, Reactor Geometry, and Time of Operation. *Ind. Eng. Chem. Res.* **1988**, *27*, 743−751.
(31) Tang, S.; Gao, S.; Wang, S.; Wang, J.; Zhu, Q.; Chen, Y.; Li, X. Characterization of CVD TiN coating at different deposition temperatures and its application in hydrocarbon pyrolysis. *Surf. Coat. Technol.* **2014**, *258*, 1060−1067.
(32) Gokulakrishnan, P.; Joklik, J.; Fuller, C. Experimental and Modeling Investigation of Pyrolytic Carbon Deposition Relevant to Fuel Film Cooling in Rocket Engines. In *55th AIAA Aerospace Sciences Meeting*, 9−13 January 2017, Grapevine: Texas, 16 pp.
(33) Reshetenko, T. V.; Avdeeva, L. B.; Ismagilov, Z. R.; Pushkarev, V. V.; Cherepanova, S. V.; Chuvilin, A. L.; Likholobov, V. A. Catalytic filamentous carbon Structural and textural properties. *Carbon* **2003**, *41*, 1605−1615.
(34) Roan, M. A.; Boehman, A. L. The effect of fuel composition and dissolved oxygen on deposit formation from potential JP-900 basestocks. *Energy Fuel* **2004**, *18*, 835−843.
(35) Pei, X.-y.; Hou, L.-y. Effect of dissolved oxygen concentration on coke deposition of kerosene. *Fuel Process. Technol.* **2016**, *142*, 86−91.
(36) Hagen, J. Heterogeneously Catalyzed Processes in Industry. In *Industrial Catalysis: A Practical Approach*, 2nd ed.; Willey-VCH Verlag GmbH&Co. KGaA; Weinheim, Germany, 2006; pp. 264.
(37) Zabarnick, S.; Mick, M. S.; Striebich, R. C.; Grinstead, R. R. Model Studies of Silylation Agents as Thermal-Oxidative Jet Fuel Additives. *Energy Fuel* **1999**, *13*, 154−159.
(38) Vander Wal, R. L.; Byrg, V. M. *Chemistry Characterization of Jet Aircraft Engine Particulate by XPS: Results From APEX III*. NASA/CR—2014−218293.
(39) Park, Y.-J.; Song, H.-J.; Kim, I.; Yang, H.-S. Surface characteristics and bioactivity of oxide film on titanium metal formed by thermal oxidation. *J. Mater. Sci. Mater. Med.* **2007**, *18*, 565−575.
(40) Zhang, B. B.; Wang, B. L.; Li, L.; Zheng, Y. F. Corrosion behavior of Ti−5Ag alloy with and without thermal oxidation in artificial saliva solution. *Dent. Mater.* **2011**, *27*, 214−220.
(41) Güleryüz, H.; Ċimenoğlu, H. Effect of thermal oxidation on corrosion and corrosion−wear behaviour of a Ti−6Al−4V alloy. *Biomaterials* **2004**, *25*, 3325−3333.
(42) Wen, M.; Wen, C.; Hodgson, P.; Li, Y. Improvement of the biomedical properties of titanium using SMAT and thermal oxidation. *Colloids Surf., B* **2014**, *116*, 658−665.
(43) Altin, O.; Eser, S.; James, A. R.; Xi, X. Ti and Al oxide coatings on Inconel 718 against metal sulfide formation and carbon deposition from heated JP-8 fuel. *Prepr. Pap.-Am. Chem. Soc., Div. Fuel Chem.* **2004**, *49*, 778−780.
(44) Yang, C.; Liu, G.; Wang, X.; Jiang, R.; Wang, L.; Zhang, X. Preparation and Anticoking Performance of MOCVD Alumina Coatings for Thermal Cracking of Hydrocarbon Fuels under Supercritical Conditions. *Ind. Eng. Chem. Res.* **2012**, *51*, 1256−1263.

DOI: 10.1021/acsomega.8b03576
ACS Omega 2019, 4, 8255−8273